A&A 506, 1341–1350 (2009)
DOI: 10.1051/0004-6361/200912570


Astronomy & Astrophysics

# Analysis of hydrogen-rich magnetic white dwarfs detected in the Sloan Digital Sky Survey⋆

B. Külebi[1], S. Jordan[1], F. Euchner[2], B. T. Gänsicke[3], and H. Hirsch[4]

[1] Astronomisches Rechen-Institut, Zentrum für Astronomie der Universität Heidelberg, Mönchhofstrasse 12-14, 69120 Heidelberg, Germany
e-mail: bkulebi@ari.uni-heidelberg.de
[2] Swiss Seismological Service, ETH Zurich, Sonneggstrasse 5, 8092 Zurich, Switzerland
[3] Department of Physics, University of Warwick, CV4 7AL Coventry, UK
[4] Dr.-Remeis-Sternwarte, Sternwartstrasse 7, 96049 Bamberg, Germany

Received 25 May 2009 / Accepted 8 July 2009

**ABSTRACT**

*Context.* A large number of magnetic white dwarfs discovered in the SDSS have so far only been analyzed by visual comparison of the observations with relatively simple models of the radiation transport in a magnetised stellar atmosphere.
*Aims.* We model the structure of the surface magnetic fields of the hydrogen-rich white dwarfs in the SDSS.
*Methods.* We calculated a grid of state-of-the-art theoretical optical spectra of hydrogen-rich magnetic white dwarfs (WDs) with magnetic field strengths of between 1 MG and 1200 MG for different angles between the magnetic field vector and the line of sight, and for effective temperatures between 7000 K and 50 000 K. We used a least squares minimization scheme with an evolutionary algorithm to find the best-fit magnetic field geometry of the observed data. We used centered dipoles or dipoles that had been shifted along the dipole axis to model the coadded SDSS fiber spectrum of each object.
*Results.* We analyzed the spectra of all known magnetic hydrogen-rich (DA) WDs from the SDSS (97 previously published, plus 44 newly discovered) and also investigated the statistical properties of the magnetic field geometries of this sample.
*Conclusions.* The total number of known magnetic white dwarfs has already been more than tripled by the SDSS and more objects are expected after more systematic searches. The magnetic fields have strengths of between ≈1 and 900 MG. Our results further support the claims that Ap/Bp population is insufficient in generating the numbers and field strength distributions of the observed MWDs, and that of either another source of progenitor types or binary evolution is needed. Clear indications of non-centered dipoles exist in about ∼50%, of the objects which is consistent with the magnetic field distribution observed in Ap/Bp stars.

**Key words.** stars: white dwarfs – stars: magnetic fields – stars: atmospheres

## 1. Introduction

White dwarfs with magnetic field strengths of between $10^4$ and $10^9$ G are understood to represent more than 10% of the total population of white dwarfs (Liebert et al. 2003). The Sloan Digital Sky Survey (SDSS), the largest spectroscopic survey carried out to date, has discovered thousands of new white dwarfs, among them 102 with magnetic fields (MWDs) (Gänsicke et al. 2002; Schmidt et al. 2003; Vanlandingham et al. 2005). After the analysis of data release 3 (DR3), the number of known magnetic white dwarfs had increased from 65 (Wickramasinghe & Ferrario 2000; Jordan 2001) to 167 (Kawka et al. 2007). The first seven magnetic DAs (DAHs) uncovered from SDSS were visually identified in the area of the initial early data release (EDR Gänsicke et al. 2002). Schmidt et al. (2003) added 46 objects in the DR1, 38 of them DAH, plus three new magnetic helium rich WDs (DBH), and five new MWDs with metallic and molecular lines. Vanlandingham et al. (2005) reported on 49 additional new MWDs from the DR2 and DR3, specifically 46 new DAH, two new DQAs and one DQ with molecular bands.

Schmidt et al. (2003) and Vanlandingham et al. (2005) determined the field strengths and the inclinations of the magnetic dipoles by visually comparing the observed spectra with model spectra. They used an extension of the modeling method of Latter et al. (1987) accounted for the effect of the change of magnetic field strength on line depths and the variation in the field strength over the stellar surface for only the unpolarized radiation flux, namely Stokes parameter $I$. Their analyzes with this simplified method of radiation transport resulted in dipolar field strengths for the SDSS MWDs of between 1.5 MG and ∼1000 MG. Including the pre-SDSS, formerly known as MWDs, their sample consisted of 111 MWDs, 97 being classified as DAHs.

In this work, we present the reanalysis of data of SDSS DAHs detected by Gänsicke et al. (2002), Schmidt et al. (2003), and Vanlandingham et al. (2005), plus the analysis of data for 44 new detection from all SDSS data until DR7 (DR4 until DR7 were not scanned systematically for MWDs).

## 2. SDSS data

SDSS investigates five-band photometry of the northern Galactic polar cap using the 2.5 m telescope at Apache Point, New Mexico, with its special purpose instruments (Fukugita et al. 1996). Follow-up spectroscopy of many stars is also performed with the twin dual-beam spectrographs (3900–6200 and

⋆ Appendix A and Table 3 are only available in electronic form at http://www.aanda.org

5800–9200 Å, $\lambda/\Delta\lambda \sim 1800$), in particular of blue objects such as white dwarfs and hot subdwarfs (Harris et al. 2003; Kleinman et al. 2004). Since the energy distribution of strongly magnetic white dwarfs can differ from nonmagnetic ones, MWDs are found not only in the SDSS color categories for white dwarfs or blue horizontal-branch stars, but may also fall into the color categories for quasars (QSOs), "serendipitous blue objects", and hot subdwarfs. Based on their colors, objects are assigned to fibers for follow-up spectroscopic investigations (for spectroscopic target selection, see Stoughton et al. 2002).

To identify magnetic white dwarfs from these samples, different techniques were used. For white dwarfs selected by color cuts in the *u-g* versus *g-r* color–color diagram, Gänsicke et al. (2002) and Schmidt et al. (2003) used visual inspection. In the work by Vanlandingham et al. (2005), visual identification was complemented with the *autofit* process (Kleinman et al. 2004), which fits spectra and photometry of hydrogen and helium white dwarfs to theoretical models. We note that white dwarfs with magnetic fields above 3 MG are flagged because of the poor $\chi^2$ fits in the *autofit* process and MWDs with weaker magnetic fields might therefore be overlooked (Vanlandingham et al. 2005).

In addition to the data from the former SDSS MWD papers (DR1-DR3), we analyzed new data of nineteen additional objects from the HYPERMUCHFUSS (HYPER velocity or Massive Unseen Companions of Hot Faint Under-luminous Stars Survey; see Tillich et al. 2009). This survey aims to detect high velocity underluminous B stars and white dwarfs. The candidates were chosen by the selection criterion $(u–g) < 0.4$ and $(g–r) < 0.1$, and spectral fits were performed to determine the radial velocity. Some objects showed formally very high negative radial velocities ($\leq -100\,\mathrm{km\,s^{-1}}$) but turned out toward be DAHs. The reason for this is that the higher-order Balmer lines of magnetic white dwarfs are shifted systematically to the blue, even for relatively small magnetic fields ($\leq$20 MG), because of the quadratic Zeeman effect, which mimicks a high radial velocity. Additionally, 34 DAHs were serendipitously found in the course of a visual inspection of blue stellar objects from DR7. The total number of DAHs from SDSS is likely to increase yet further once a systematic search of all DR7 spectra has been carried out.

The one-dimensional spectra used in this work were generated by SDSS's spectroscopic pipeline `spectro2d` and downloaded from the Data Archive Server.

## 3. Analysis

Our model spectra are calculated with a radiative transfer code for magnetized white dwarf atmospheres that, for a given temperature and pressure structure of a model atmosphere ($T_{\rm eff}$, $\log g$) and a given magnetic field vector with respect to the line of sight and the normal on the surface of the star, calculates both theoretical flux and polarization spectra (see Jordan 1992; Jordan & Schmidt 2003).

To increase efficiency, we pre-computed a three-dimensional grid of Stokes $I$ and $V$ ($V$ spectra were not used due to a lack of polarization measurements) model spectra with effective temperature $7000\,\mathrm{K} \leq T_{\rm eff} \leq 50\,000\,\mathrm{K}$ 14 steps, magnetic field strength $1\,\mathrm{MG} \leq B \leq 1.2\,\mathrm{GG}$ in 1200 steps, and 17 different directions of $\psi$ relative to the line of sight, as the independent variables (9 entries, equally spaced in $\cos\psi$). All spectra were calculated for a surface gravity of $\log g = 8$. Since no polarization information is available from the SDSS, our analysis is limited to the flux spectra (Stokes parameter $I$). Limb darkening is accounted for by a simple linear scaling law (see Euchner et al. 2002).

The magnetic field geometry of the DAHs was determined with a modified version of the code developed by Euchner et al. (2002). This code calculates the total flux (and circular polarization) spectra for an arbitrary magnetic field topology by adding up appropriately weighted model spectra for a large number of surface elements and then evaluating the goodness of fit. Magnetic field geometries are accounted for by multipole expansions of the scalar magnetic potential. The individual multipole components may be independently oriented with respect to the rotation axis of the white dwarf and offset with respect to its center, allowing in principle the modeling of rather complex surface field topologies. Additional free parameters are the white dwarf effective temperature and the inclination of the rotation axis with respect to the line of sight. Observed spectra can be fitted using an evolutionary algorithm (Rechenberg 1994) with a least squares quality function.

In addition to the Zeeman effect, Stark broadening must be considered. When the electric and magnetic fields are parallel, Friedrich et al. (1994) estimated the effect on stationary line components, which are transitions that vary slowly in wavelength for large intervals of magnetic field strengths. Stationary lines are more pronounced than non-stationary lines, since they are not smeared out extensively by the variation in the magnetic field strength over the stellar surface.

However, no atomic data for hydrogen in the presence of both a magnetic and electric field are available for arbitrary strengths and arbitrary angles between two fields. Therefore, only a crude approximation (see Jordan 1992) is used in our model and systematic uncertainties are unavoidable, particularly in the low-field regime ($\leq$5 MG), where the Stark effect dominates. Consequently, effective temperatures and surface gravities derived by fitting the Balmer lines alone are less reliable than in the case of non-magnetic white dwarfs. This may also produce disagreements with temperature estimates derived from the continuum slope.

Time-resolved analysis for rotating single magnetic white dwarfs was instrumental in determining rather complex field structures (e.g., VLT observations by Euchner et al. 2002, 2005, 2006). However, this usually relies on the preliminary knowledge of period, which is usually derived separately by photometry. Although the individual SDSS fiber spectra exists with 15 min exposure time, because of a lack of information about spin period, we constrained ourselves to the coadded spectra, which includes 3 or more individual spectra with total exposure times of at least 45 min. With the possible exception of a few bright objects, the signal-to-noise ratio of the individual spectra would not be sufficient to find indications of rotational changes. Therefore, we had to restrict ourself to simple models for the magnetic field geometry, namely centered magnetic dipoles with only two free parameters or to dipoles offset along the magnetic axis with three free parameters. These parameters are the magnetic dipole field strength $B_{\rm p}$, and the inclination of the dipole axis $i$ for the centered dipole. For the offset dipole, there is an additional offset parameter along the magnetic axis $z_{\rm off}$ in terms of the stellar radius. For the 97 DAHs analyzed, we used the literature values for $T_{\rm eff}$, which were determined by comparison to the theoretical non-magnetic DA colors in the *u-g* vs. *g-r* plane (Schmidt et al. 2003; Vanlandingham et al. 2005). The temperature of the new DAHs presented in Table 1 were estimated with synthetic SDSS color–color diagrams by Holberg & Bergeron (2006)[1], assuming that the influence of the magnetic field on the

[1] http://www.astro.umontreal.ca/~bergeron/CoolingModels/

**Table 1.** Photometric properties of the new confirmed DAHs and their temperatures.

| MWD (SDSS+) | Plate-MJD-FiberID | $u$/mag | $g$/mag | $r$/mag | $i$/mag | $z$/mag | $T_{\rm eff}$/K |
|---|---|---|---|---|---|---|---|
| J023420.63+264801.7 | 2399-53764-559 | 18.70 | 18.38 | 18.59 | 18.76 | 19.03 | 13 500 |
| J031824.19+422651.0 | 2417-53766-568 | 18.59 | 18.23 | 18.32 | 18.43 | 18.67 | 10 500 |
| J032628.17+052136.3 | 2339-53729-515 | 18.69 | 18.93 | 19.30 | 19.60 | 19.61 | 25 000 |
| J033320.36+000720.6 | 0415-51879-485 | 17.07 | 16.52 | 16.39 | 16.35 | 16.44 | 7000[1,2] |
| J074924.91+171355.4 | 2729-54419-282 | 18.78 | 18.78 | 19.13 | 19.44 | 19.64 | 20 000 |
| J075234.96+172525.0 | 1920-53314-106 | 18.78 | 18.44 | 18.44 | 18.50 | 18.64 | 9000 |
| J080359.93+122943.9 | 2265-53674-033 | 17.24 | 17.23 | 17.53 | 17.83 | 18.08 | 9000 |
| J081716.39+200834.8 | 2082-53358-444 | 18.91 | 18.34 | 18.15 | 18.12 | 18.23 | 7000 |
| J083448.63+821059.1 | 2549-54523-135 | 18.07 | 18.32 | 18.74 | 19.06 | 19.49 | 27 000 |
| J083945.56+200015.7 | 2277-53705-484 | 18.11 | 17.83 | 18.11 | 18.36 | 18.66 | 15 000[3] |
| J085106.12+120157.8 | 2430-53815-229 | 17.35 | 16.96 | 17.14 | 17.30 | 17.56 | 11 000 |
| J085523.87+164059.0 | 2431-53818-522 | 18.78 | 18.55 | 18.80 | 19.05 | 19.32 | 15 500 |
| J085550.67+824905.3 | 2549-54523-066 | 18.40 | 18.60 | 18.91 | 19.23 | 19.46 | 25 000 |
| J091005.44+081512.2 | 1300-52973-639 | 17.38 | 17.54 | 17.96 | 18.28 | 18.65 | 25 000 |
| J091833.32+205536.9 | 2288-53699-547 | 18.73 | 18.41 | 18.66 | 18.92 | 19.22 | 14 000 |
| J093409.90+392759.3 | 1215-52725-241 | 18.72 | 18.35 | 18.40 | 18.50 | 18.55 | 10 000 |
| J094235.02+205208.3 | 2292-53713-019 | 18.41 | 18.42 | 18.80 | 19.05 | 19.26 | 20 000 |
| J100657.51+303338.1 | 1953-53358-415 | 19.22 | 18.83 | 18.90 | 19.04 | 19.18 | 10 000 |
| J100759.80+162349.6 | 2585-54097-030 | 18.01 | 17.70 | 17.80 | 17.96 | 18.19 | 11 000 |
| J101428.09+365724.3 | 52993-1426-021 | 19.26 | 18.87 | 18.97 | 19.09 | 19.43 | 10 500 |
| J102220.69+272539.8 | 2350-53765-543 | 20.47 | 20.05 | 20.16 | 20.38 | 20.69 | 11 000 |
| J102239.06+194904.3 | 2374-53765-544 | 19.43 | 19.01 | 19.01 | 19.11 | 19.13 | 90 00 |
| J103532.53+212603.5 | 2376-53770-534 | 17.98 | 17.40 | 17.23 | 17.19 | 17.21 | 7000[2] |
| J105709.81+041130.3 | 0580-52368-274 | 18.09 | 17.67 | 17.58 | 17.60 | 17.70 | 8000 |
| J112030.34-115051.1 | 2874-54561-512 | 18.65 | 18.73 | 19.05 | 19.34 | 19.75 | 20 000 |
| J112257.10+322327.8 | 1979-53431-512 | 19.60 | 19.37 | 19.50 | 19.68 | 19.92 | 12 500 |
| J112328.49+095619.3 | 1222-52763-625 | 18.15 | 17.70 | 17.74 | 17.87 | 18.02 | 9500 |
| J113215.38+280934.3 | 2219-53816-329 | 17.50 | 16.99 | 16.88 | 16.87 | 16.92 | 7000[2] |
| J124836.31+294231.2 | 2457-54180-112 | 18.44 | 17.80 | 17.59 | 17.54 | 17.56 | 7000[2] |
| J125434.65+371000.1 | 1989-53772-41 | 16.01 | 15.97 | 16.35 | 16.64 | 16.95 | 10 000 |
| J125715.54+341439.3 | 2006-53476-332 | 17.14 | 16.78 | 16.81 | 16.92 | 17.11 | 8500 |
| J134820.79+381017.2 | 2014-53460-236 | 17.26 | 17.54 | 18.04 | 18.33 | 18.70 | 35 000 |
| J140716.66+495613.7 | 1671-53446-453 | 19.03 | 19.13 | 19.43 | 19.75 | 19.97 | 20 000 |
| J141906.19+254356.5 | 2131-53819-317 | 17.80 | 17.41 | 17.46 | 17.53 | 17.69 | 9000 |
| J143019.05+281100.8 | 2134-53876-423 | 18.03 | 17.68 | 17.68 | 17.74 | 17.92 | 9000 |
| J151130.17+422023.0 | 1291-52738-615 | 18.20 | 17.98 | 18.01 | 18.20 | 18.48 | 9500 |
| J151415.65+074446.5 | 1817-53851-534 | 19.16 | 18.84 | 18.88 | 18.99 | 18.88 | 10 000 |
| J152401.60+185659.2 | 2794-54537-410 | 18.39 | 18.15 | 18.34 | 18.54 | 18.8 | 13 500 |
| J153843.10+084238.2 | 1725-54266-297 | 18.24 | 17.90 | 17.94 | 18.22 | 18.20 | 9500 |
| J154305.67+343223.6 | 1402-52872-145 | 18.08 | 18.32 | 18.75 | 19.10 | 19.46 | 25 000 |
| J165249.09+333444.9 | 1175-52791-095 | 19.11 | 18.63 | 18.63 | 18.65 | 18.92 | 9000 |
| J202501.10+131025.6 | 2257-53612-167 | 18.91 | 18.76 | 19.07 | 19.28 | 19.74 | 17 000 |
| J220435.05+001242.9 | 0372-52173-626 | 19.66 | 19.38 | 19.47 | 19.54 | 19.71 | 22 000 |
| J225726.05+075541.7 | 2310-53710-420 | 17.09 | 17.11 | 17.31 | 17.44 | 17.65 | 40 000 |

[1] HE 0330-0002.
[2] The temperature from fits to the color–color diagram is uncertain.
[3] WD 0837+199 (LB 393, EG 61).
The columns indicate the SDSS name of the object; the plate, Modified Julian Date, and fiber ids of the observations; the SDSS photometric magnitudes $u$, $g$, $r$, $i$, $z$; and finally the temperatures derived from their colors.

temperature determination is small, which is not always the case (see Schmidt et al. 1986; Gänsicke et al. 2001, and Sect. 4.2).

All fits have reduced $\chi^2$ values between 0.8 and 3.0 except for some high-field objects that obviously deviate from the assumed dipole geometry (see Sect. 4). We use the error calculation method of Zhang et al. (1986), which assumes that a small change in $\chi^2$ could be approximated by a linear expansion of the covariance matrix; for complex $\chi^2$ topologies, this approximation is inaccurate, final error in the inclination is often very large.

Final fit parameters with errors are noted in Table 3. In Figs. 1 and 2, we show fits of 12 DAHs, as an example. All of the fits to our remaining spectra can be found in the online version of this article (Figs. A.3–A.23 for the other DAHs).

## 4. Results

### 4.1. Individual objects

Three objects analyzed by Schmidt et al. (2003) and Vanlandingham et al. (2005) were omitted in this work. *SDSSJ05959.56+433521.3* (*G111-49*) was listed by Schmidt et al. (2003) as a DAH, but is a carbon-rich (DC) MWD (Putney 1995). *SDSSJ084716.21+148420.4* is a DAH+DB binary, in which the helium component in the spectrum is quite strong.

This dilution of the hydrogen features prevented an accurate analysis of this object by our code. Finally, we were unable to model the SDSS spectrum of *J220029.08-074121.5* due to the lack of any discernible features.

Emission lines were found in *SDSSJ102220.69+272539.8* and *SDSSJ102239.06+194904.3* (the latter being shown in Fig. 1) that are very similar to those of *SDSSJ121209.31-+013627.7* which could indicate that these objects are EF Eri like, magnetic cataclysmic variables with a brown dwarf companion (Schmidt et al. 2005; Debes et al. 2006; Burleigh et al. 2006; Farihi et al. 2008).

The spectra of the high-field objects *SDSSJ224741.41-+145638.8* and *SDSSJ101805.04+01123.5* (PG 1015+014, shown in Fig. 1) cannot be reproduced particularly well. At higher field strengths (>50 MG), the spectra become very sensitive to the details of the magnetic field geometry, as was demonstrated by Euchner et al. (2002, 2005, 2006). The deviations of the observed spectra from our theoretical spectra assuming (offset) dipole models, therefore imply a magnetic field geometry that is more complex than a shifted dipole. A more comprehensive analysis of *SDSSJ101805.04+01123.5* showed that individually tilted and off-centered zonal multipole components with field strengths in the range 50–90 MG is needed to represent the global magnetic field (Euchner et al. 2006), which was consistent with our analysis.

The colors of MWDs with high field strengths (>50 MG) are known to differ from non-magnetic white dwarf colors because the absorption in their spectral features as noted in Sect. 2. This behavior also affects temperature determinations from color–color diagrams. The analysis of *SDSSJ224741.41+145638.8* by Euchner et al. (2006) inferred an effective temperature of $T_{\rm eff}$ = 10000 ± 1000 K, unlike $T_{\rm eff}$ = 12000 K that is derived from color–color diagrams. We used 10 000 K for our models, and this value provided better results, especially on the basis of line depths. When color–derived effective temperatures were used, a similar discrepancy with the slopes and line depths was also observed in *SDSSJ224741.41+145638.8*. The temperature 17 000 K was used in modeling by Schmidt et al. (2003), but the colors of *SDSSJ224741.41+145638.8* are outside the Holberg & Bergeron (2006) grid of $\log g - T_{\rm eff}$ in $u$-$g$ – $g$-$r$ plane. In our procedure, we accomplished the best result with 50 000 K for this object on the basis of slope and line depths. On the other hand, some high-field objects in our sample such as *SDSSJ135141.13-+541947* (Fig. 1) were fitted well and this discrepancy between the temperature derived by either colors or spectral fits was not observed.

In some of the optimal fits, the line depths of the observed and computed spectra strongly differ. These unsatisfactory fits are caused by two different kind of problems: either of the $\sigma^{\pm}$ components was shallower than expected on the basis of their sharp $\pi$ counterparts in observed spectra, with respect to the models; or both $\sigma^{\pm}$ and $\pi$ components of the lines were too shallow.

Sharp line cores within shallow wings in the spectra was already noted for *J123414.11+124829.6* by Vanlandingham et al. (2005). It has been suggested that this might be caused by a deviation from centered dipole geometry, and our fits with offset dipole models proved to be considerably better than the centered dipole models in reduced $\chi^2$. For lower magnetic strengths (<50 MG), the smearing effect of offset dipole models affects only the $\sigma^{\pm}$ components of the lines. The reason is that in this field regime $\sigma^{\pm}$ components become more separated, while the $\pi$ components are only slightly blue-shifted with increasing field strength. Therefore smeared-out wings with sharp-line cores can be synthesized by adding spectra with a wider range of magnetic field strength values. Dipole models with offsets can generate such extended magnetic field distributions (see Sect. 4.2). Our fit to *J123414.11+124829.6* was considerably tighter but we did not reproduce the exact profile. Another possible explanation of this spectrum is the contribution from a non-magnetic DA, which would dilute the $\sigma^{\pm}$ components causing an increased contrast between the wings and line cores. Offset dipole models improved our fits, although further analysis is needed to differentiate between the effect of geometry and the possible contribution from a non-magnetic DA.

The other case, *J113756.50+574022.4* (see Fig. 1), has very shallow features with discernible magnetic wings. Neither a complicated geometry nor a change in effective temperature can explain its lack of line depth. Nevertheless, the magnetic field strength could be derived from the extent of the wings. We propose that this object is an unresolved spectroscopic binary (e.g., with DA+DC components), since in these situations hydrogen line strengths are known to be suppressed by the other component (Bergeron et al. 1990; Liebert et al. 1993). The other objects with shallow features that belong to this category are: *J084716.21+484220.4*, *J090632.66+080716.0*, *J113215.38+280934.3*, *J103532.53+212603.5*, *J112328.49+095619.3*, *J124806.38+410427.2*, *J141906.19+254356.5*.

One additional interesting outcome of our work was the results of modeling of *J033320.36+000720.6*, which was formerly identified in the Hamburg/ESO survey for bright quasars as HE 03330-0002 (Reimers et al. 1998). Its magnetic properties were confirmed by Schmidt et al. (2001) by circular polarimetry; nevertheless, the modeling of the HE 03330-0002 was previously impossible, since the transitions in its spectrum were not understood to be caused either hydrogen or because of helium transitions. Although *J033320.36+000720.6* was discovered in the EDR, because of this lack of knowledge about its atmosphere Gänsicke et al. (2002) did not attempt to model its data with a pure hydrogen atmosphere.

However, we noted that some of the lines in the spectrum of *J033320.36+000720.6* possibly coincided with hydrogen stationary lines. Therefore we decided to model the spectrum with a 7000 K DAH atmosphere. Our initial fits with a centered dipole inferred a dipolar field strength of ~850 MG (see Fig. 2), which reproduced the position but not the depths of the three transitions. More careful modeling with an offset dipole showed that the mean field strength over the visible surface is far more concentrated than for a regular dipole field geometry. Figure 4 shows that the mean field strengths are predominantly in the interval 390–470 MG. When we consider the apparent peak value of this distribution, we infer line positions for three lines in the spectrum that are commensurate with those of H$\alpha$ transitions (see Table 2).

The pure hydrogen atmosphere was unable to produce the red part ($\lambda$ < 5500 Å) of the spectrum. There appear to be additional opacity contributions from different species of elements, to both the continuum and the features.

### 4.2. Magnetic field geometry

We have modeled a large sample of DAHs with dipole magnetic fields offset from the magnetic axis. However, the visualization of these model parameters is not straightforward. The effect of the dipole offset on the model spectrum depends on both inclination and the polar field strength. However, the polar field strength is not representative of the global magnetic field on the visible

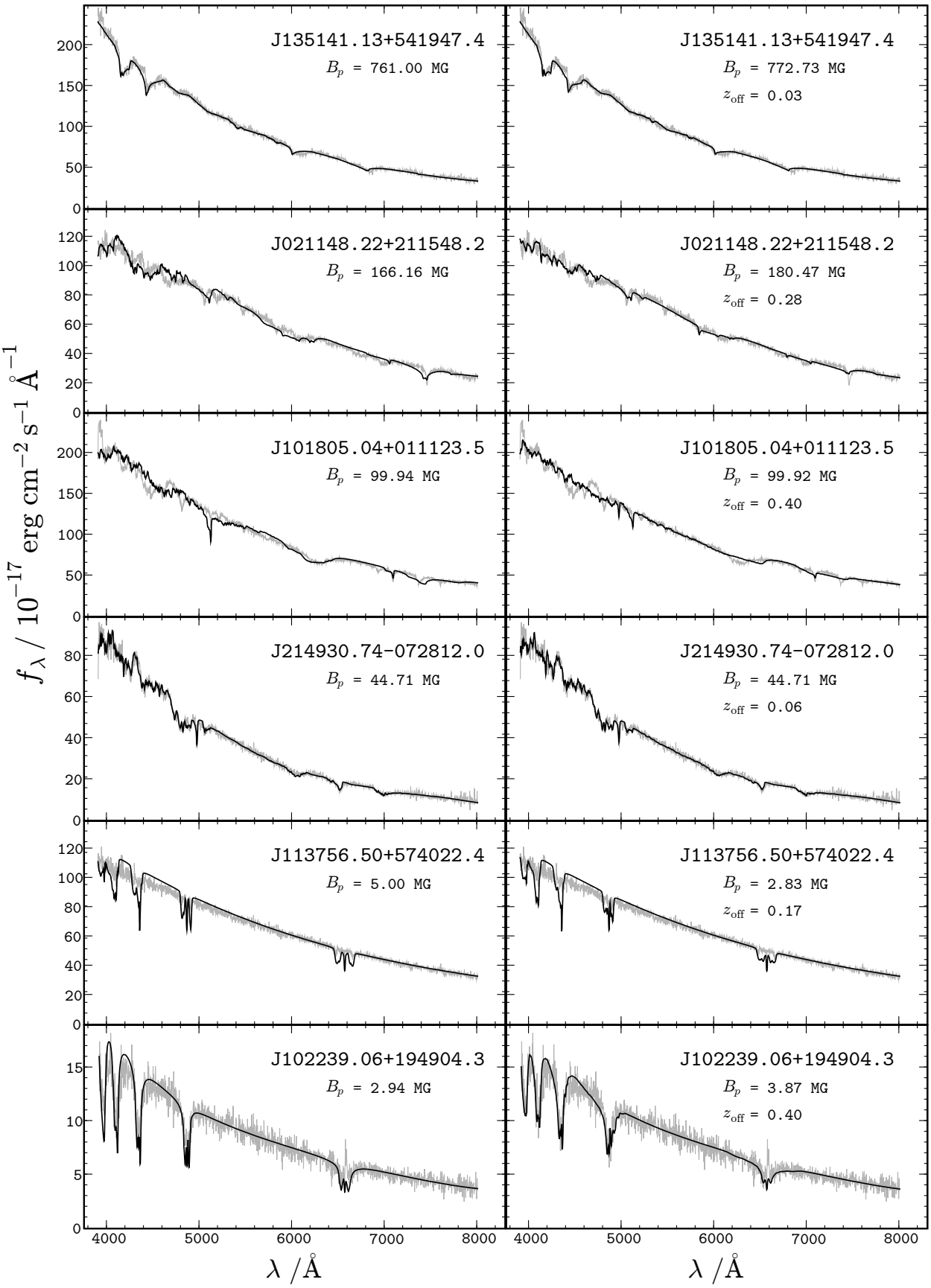


**Fig. 1.** Fits of observed spectra of DAHs from the SDSS to centered magnetic dipoles with a polar field strength $B_{\rm p}$ (*left*) and dipoles shifted by $z_{\rm off}$ stellar radii along the dipole axis (*right*). Representative fits and objects mentioned throughout the article are chosen. The color version of this figure (Fig. A.1) and the remaining 128 fits can be found in the online version of this paper.

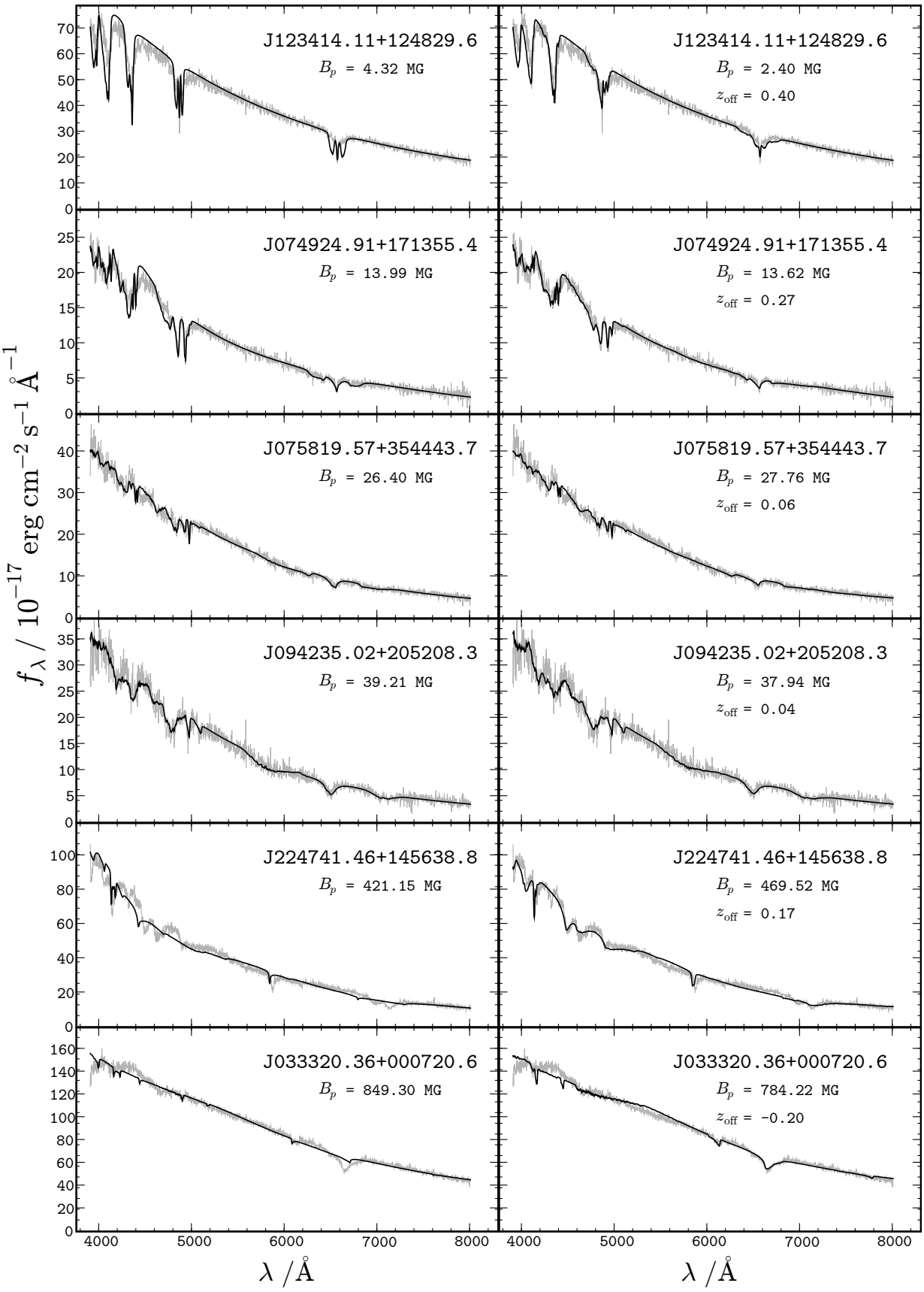


**Fig. 2.** Fits of observed spectra of DAHs from the SDSS to centered magnetic dipoles with a polar field strength $B_{\rm p}$ (*left*) and dipoles shifted by $z_{\rm off}$ stellar radii along the dipole axis (*right*). Representative fits and objects mentioned throughout the article are chosen. The color version of this figure (Fig. A.2) and the remaining 128 fits can be found in the online version of this paper.

**Table 2.** The hydrogen transitions of SDSSJ033320.36+000720.6 and their wavelengths at 446.5 MG.

| Line | $nlm - n'l'm'$ | $\lambda$(Å) |
|---|---|---|
| H$\alpha$ | $2s_0$–$3p_0$ | 6113.05 |
| H$\alpha$ | $2s_0$–$3p_{-1}$ | 7710.91 |
| H$\alpha$ | $2p_{-1}$–$3d_{-2}$ | 6647.76 |

surface if the offsets are large. The most direct way to investigate a model geometry is to construct a diagram of the angle between the line-of-sight and the local magnetic field vector versus the magnetic field strength plot i.e., equivalent to the ZEeman BRoadening Analysis (ZEBRA) plots of (Donati et al. 1994). In our case, since we did not have polarization data, we only considered the magnetic field strength distribution histograms for simplicity.

In general, the effect of the offset dipole models is to either extend or reduce the range of magnetic field strengths across, the visible surface of the MWD, which is a fixed factor of two for centered dipole models (see Fig. 3). For offset dipoles, the range depends on both the values of $B_p$ and the inclination $i$. To quantify the difference between the centered and off-centered dipole models, we determined the average and the standard deviation $\sigma$ of the distribution of the magnetic fields for the parameters of our best-fit solution. The relative change in the standard deviations $\sigma_{\rm centered}$ and $\sigma_{\rm offset}$ is given by $\sigma_{\rm rel} = \frac{\sigma_{\rm offset} - \sigma_{\rm centered}}{\sigma_{\rm centered}}$.

The value $\sigma_{\rm rel} = 0$ indicates that the widths of the centered and offset dipole models are the same, $\sigma_{\rm rel} < 0$ indicates that more concentrated than a dipole field, and for $\sigma_{\rm rel} > 0$ the distribution of field strengths is more extended.

To present the magnetic field geometry of our sample, we plotted the histogram of $\sigma_{\rm rel}$ values for all known SDSS DAHs, except those discussed in Sect. 4.1 as possible binaries (Fig. 5). The average $\sigma_{\rm rel}$ for this sample was found to be 2.18. This implies that even for SDSS spectra of quite low signal-to-noise ratio, there is an overall tendency towards non-dipolarity for our sample of white dwarfs.

### 4.3. General discussion

Overall, our results are consistent with previous analyzes of DAHs (see Fig. 6), which shows that simple atmosphere models with pre-assumed dipole magnetic values are good approximations for these objects. In all cases, offset dipole models resulted in significantly tighter fits than models with centered dipoles. We noted in Sect. 4.1 that for some DAHs with high fields, completely satisfactory fits cannot be achieved with offset dipole models. This is indicative of a magnetic field geometry that is more complex than a shifted dipole.

The dipole magnetic field Ohmic decay timescale is $10^{10}$ yr. Even higher multipoles can live for such a long period of time (Muslimov et al. 1995). Therefore, no significant correlation between temperature and magnetic field strength is expected if temperature is assumed to be an indicator of age (Fig. 8). This lack of correlation supports the fossil ancestry of these fields inherited from earlier stages of stellar evolution.

## 5. Conclusion

In this paper, we have analyzed 141 DAHs, 97 of which had been previously analyzed and 44 of which were being new. Gänsicke et al. (2002) conservatively estimated that the total number of MWDs would be tripled by the complete SDSS coverage. Before the end of the systematic search of the latest data releases, this expectation has already been surpassed. In addition, our consistent modeling over the data releases show that within the SDSS DAH population, there is a tendency to deviate from simple centered dipoles. There are clear indications of deviations from centered dipole models for at least 50% of the SDSS DAHs (see Fig. 5).

The distribution of the magnetic field strengths of the MWDs in the Schmidt et al. (2003) sample is concentrated in the ~5–30 MG interval. We have revised the magnetic field strengths of all known DAHs and created a histogram (Fig. 7). The values were taken from Jordan (2009), which is an extended and corrected version of Kawka et al. (2007). The same overabundance in the range ~5–30 MG discussed in Schmidt et al. (2003) is apparent in Fig. 7, but overall, SDSS has nearly tripled the number of known DAHs and hence the completeness of the total MWD population is significantly affected by SDSS biases because of this high impact of SDSS.

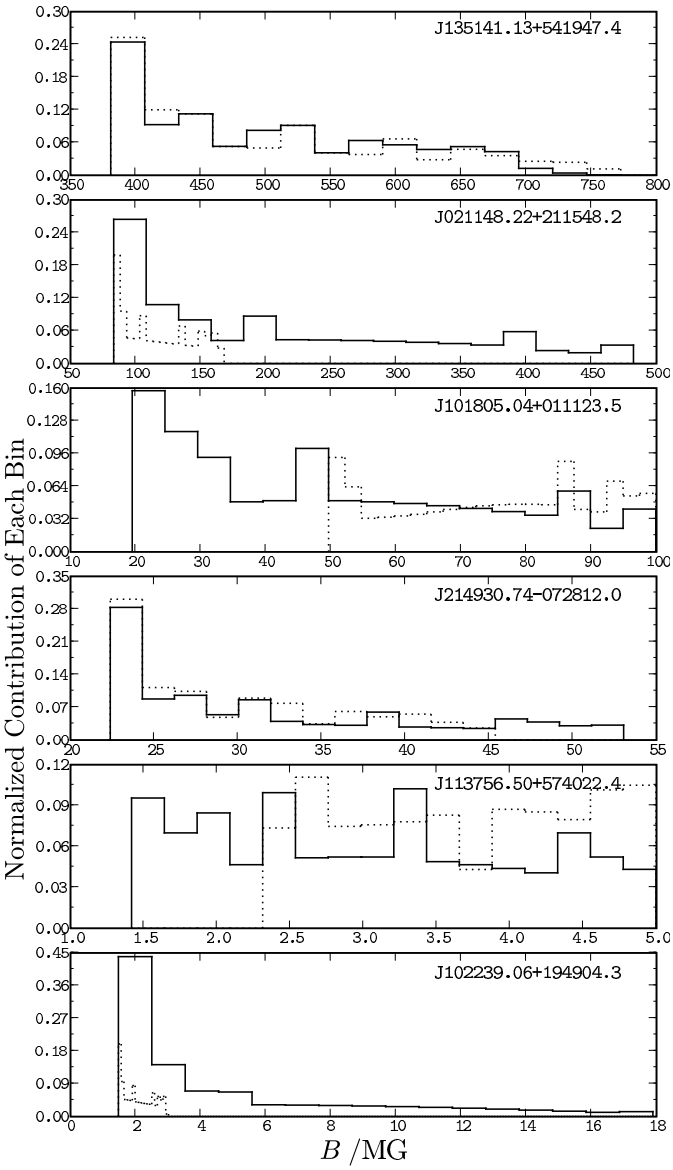


**Fig. 3.** Normalized histograms of the magnetic field strength distributions over the visible hemisphere of the star used for calculation of the synthetic spectra shown on Fig. 1. Dotted lines represent the centered dipole models, solid lines indicate dipole models with offsets.

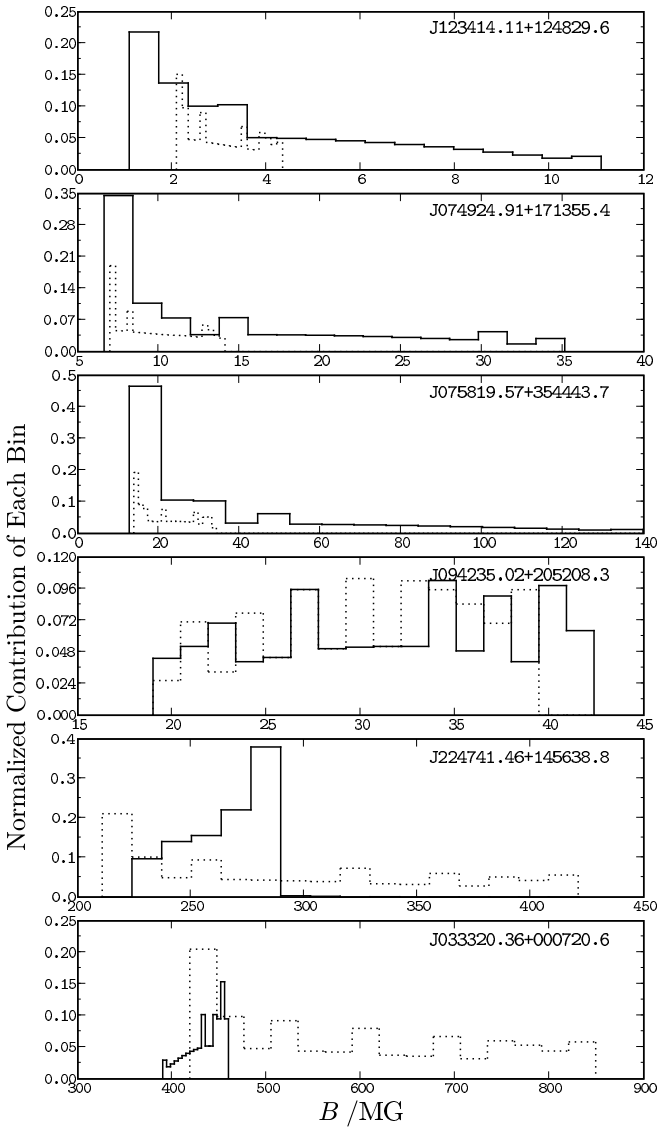


**Fig. 4.** Normalized histograms of the magnetic field strength distributions over the visible hemisphere of the star used for calculation of the synthetic spectra shown in Fig. 2. Dotted lines represent the centered dipole models, solid lines indicate dipole models with offsets.

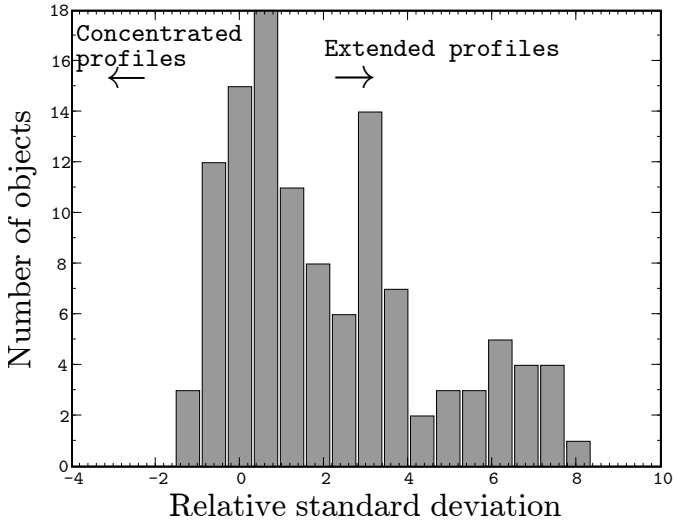


**Fig. 5.** Histogram of the relative variance $\sigma_{\rm rel}$ (see Sect. 4.2) for known SDSS MWDs. Negative $\sigma_{\rm rel}$ indicates a magnetic field strength profile of the visible surface which is more concentrated than a centered dipole, whereas positive indicates profiles that are more extended.

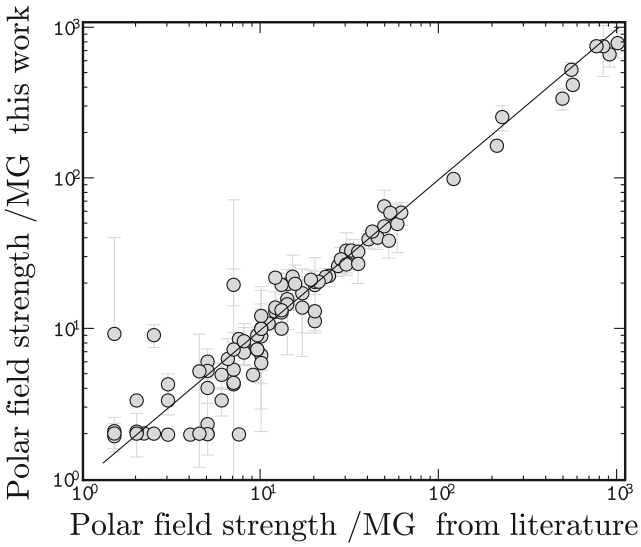


**Fig. 6.** Comparison of centered dipole magnetic field fit values in this work versus Schmidt et al. (2003), Vanlandingham et al. (2005).

High field MWDs are understood to be the remnants of magnetic Ap and Bp stars. If flux conservation is assumed, the distribution of the polar field strengths of high field MWDs should be most significant in the interval 50–500 MG. In our sample, objects with magnetic field strengths lower than 50 MG are more numerous than objects with higher magnetic field strengths (see Fig. 7). Part of this effect is caused by our biases (see Sect. 2). Nevertheless, it is consistent with previous results and supports the hypothesis that fossil magnetic fields from Ap/Bp stars alone are insufficient to produce high field MWDs (Wickramasinghe & Ferrario 2005). Aurière et al. (2007) argued that dipole magnetic field strengths of magnetic Ap/Bp stars have a "magnetic threshold" due to large-scale stability conditions, and this results in a steep decrease in the number of magnetic Ap/Bp stars below polar magnetic fields of 300 G.

A possible progenitor population of MWDs with dipolar field strengths below 50 MG, is a currently unobserved population of A and B stars with magnetic field strengths of 10–100 G. Wickramasinghe & Ferrario (2005) suggested that if ~40% of A/B stars have magnetism, this would be sufficient to explain the observed distribution of MWDs. However, the existence of this population seems to be highly unlikely, since the the investigations of Shorlin et al. (2002) and Bagnulo et al. (2006) of magnetism in this population yielded null results, for median errors of 15–50 G and 80 G, respectively. Another candidate progenitor of these MWDs with lower field strengths is the yet undetected magnetic F stars (Schmidt et al. 2003). However, this conclusion is strongly affected by SDSS MWD discovery biases.

In our work, we have quantified the deviation from centered dipoles in our sample. To test the fossil field hypothesis, one can consider the statistical properties of the fields of Ap/Bp stars. One such statistical analysis was completed by Bagnulo et al. (2002). In their work, they used the mean longitudinal field, the crossover, the mean quadratic field and the mean field modulus to invert the magnetic field structure modeled by a dipole plus quadrupole geometry (the modeling procedure is explained in depth in Bagnulo et al. 1996; Landolfi et al. 1998). The aim of

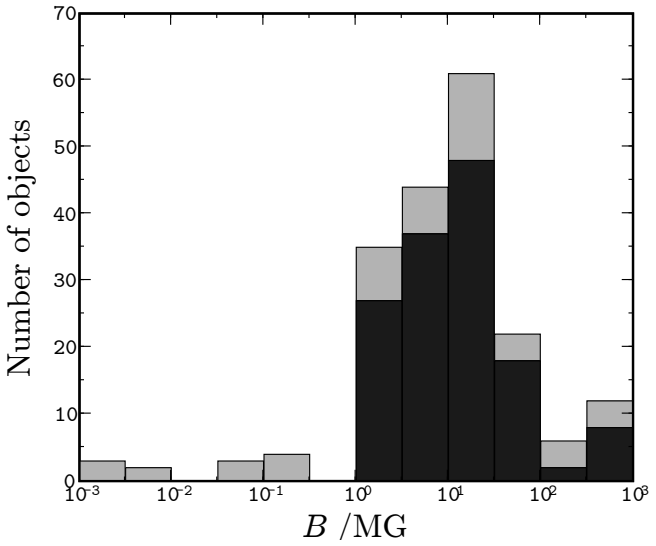


**Fig. 7.** Histogram of the known magnetic white dwarfs in equal intervals of log $B$. Gray columns represent the number of all known DAHs. Black shades represent the the contribution of SDSS to DAHs.

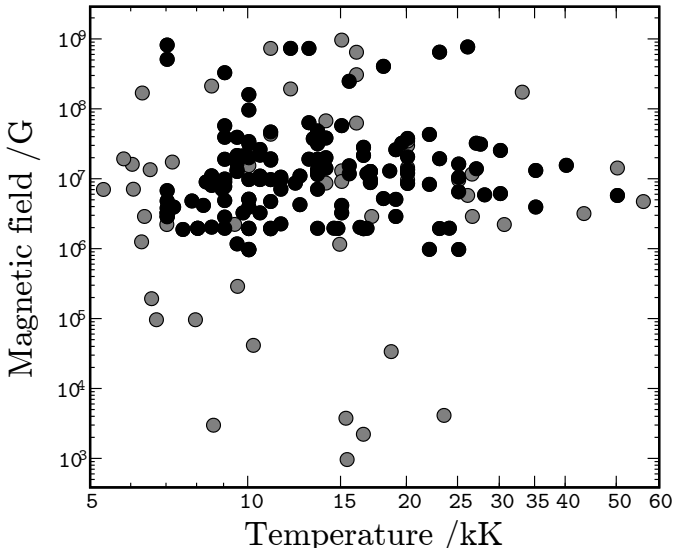


**Fig. 8.** Scatter plot of dipole magnetic field value vs temperature. While black dots represent all known SDSS DAHs, grey dots indicate the DAHs from literature that were not analyzed in this work. The random distribution of field strengths with respect to age indicator temperature is consistent with long decay timescale of DAHs with respect to their cooling age.

this analysis was to characterize the sample rather than find the best-fit solution for each object. Using the aforementioned observables, they analyzed 31 objects and derived 147 "good fit" models. These models corresponded to the minima of the $\chi^2$ hypersurfaces in their inversion procedure. Later model parameters were weighted by these reduced $\chi^2$ values when assessing their statistical properties.

Bagnulo et al. (2002) investigated the relative importance of quadrupole and dipole in the magnetic field models by plotting weighted histograms of $B_d/B_q$, where $B_d$ is the amplitude of dipole field strength ($B_p$ in this work), and $B_q$ is the amplitude of the quadrupole field strength. The main differences between our analysis and that of Bagnulo et al. (2002) was the usage of visual magnetic field distributions rather than the global magnetic field inferred from the time-resolved observations. The relationship between $B_d/B_q$ and to our relative variance parameter is not straightforward, since the structure of the total field depends on the angle between the dipole and quadrupole components. If we consider $B_d/B_q = 1$ as the point where the quadrupole component begins to dominate, 63% of the models can be considered predominantly quadrupolar (see Fig. 3 of Bagnulo et al. 2002). Hence, our conservative assessment that at least 50% of DAHs have non-dipolar fields, seems to be consistent with this result.

However one needs to be careful in considering the correspondence between the geometry between MWDs and their progenitors since theoretical models expect the field on the surface to evolve under certain conditions. Braithwaite & Spruit (2004) investigated the stable configurations of magnetic fields in stars with their magnetohydrodynamics code. Their work found that initial random fields decay within a few Alfvén timescales to a poloidal plus toroidal stable configuration. During the star's evolution, its toroidal field may diffuse outwards since the Ohmic diffusion timescale is within the order of the lifespan of an Ap/Bp star (Braithwaite & Nordlund 2006). On the Ohmic timescale, the expected initial offset-dipole configuration of the surface magnetic field evolves to a simple centered dipole. Hence, Braithwaite & Nordlund (2006) hypothesized that Ap stars with centered dipole fields are likely to be older than Ap stars with non-dipolar geometries. It is important to mention that the concentration of the field inside the star is also an important parameter, which contributes to the structure of the surface magnetic field. A highly concentrated field results in a surface field structure with higher order multiples after the internal toroidal field formation. The relative importance of the Ohmic diffusion (i.e., the age) and concentration of the initial field on the surface magnetic field structure has yet to be further investigated. Nevertheless, if the Ohmic diffusion timescale affects the lifetime of an Ap star, then it would be more relevant to compare the field configurations of an older population of Ap stars with the magnetic field distribution of MWDs. This kind of work has not yet been undertaken for Ap stars.

If we neglect the possibility that older Ap stars may behave differently from the whole sample of this group and the field structure of MWDs do not evolve as Muslimov et al. (1995) suggested (see Sect. 4.3), then the global analysis of Bagnulo et al. (2002) imply that the distribution of field structures of chemically peculiar stars and DAHs are comparable, hence supporting the fossil field hypothesis.

In addition to the isolated evolution scenario, a binary star origin was proposed by Tout et al. (2008) for generating magnetic fields in WDs. In this picture, during the evolution to the cataclysmic variables (CVs) the cores of giants experience a common envelope (CE) phase. During this phase, the orbital angular momentum is transferred to the envelope as the two cores spiral in toward each other. This process causes both differential rotation and convection within the CE, which are the key ingredients of magnetic field generation (see Tout et al. 2008, and references therein).

A consistent account of the origins of magnetic fields in WDs awaits the finalization of the complete sample of SDSS MWDs.

*Acknowledgements.* Part of this work supported by the DLR under grant 50 OR 0201. The Sloan Digital Sky Survey (SDSS) is a joint project of the University of Chicago, Fermilab, the Institute for Advanced Study, the Japan Participation Group, the Johns Hopkins University, the Max-Planck-Institut für Astronomie, New Mexico State University, Princeton University, the United States Naval Observatory, and the University of Washington. Apache Point Observatory, site of the SDSS, is operated by the Astrophysical Research Consortium. Funding for the project has been provided by the Alfred P. Sloan Foundation, the SDSS

member institutions, the National Aeronautics and Space Administration, the National Science Foundation, the U.S. Department of Energy, Monbusho, and the Max Planck Society. The SDSS World Wide Web site is http://www.sdss.org/ B.K. would like to acknowledge support from the International Max-Planck Research School (IMPRS) for Astronomy and Cosmic Physics at the University of Heidelberg, and Heidelberg Graduate School of Fundamental Physics (HGSFP).

## References

Aurière, M., Wade, G. A., Silvester, J., et al. 2007, A&A, 475, 1053
Bagnulo, S., Landi degl'Innocenti, M., & Landi degl'Innocenti, E. 1996, A&A, 308, 115
Bagnulo, S., Landi Degl'Innocenti, M., Landolfi, M., & Mathys, G. 2002, A&A, 394, 1023
Bagnulo, S., Landstreet, J. D., Mason, E., et al. 2006, A&A, 450, 777
Bergeron, P., Liebert, J., & Greenstein, J. L. 1990, ApJ, 361, 190
Braithwaite, J., & Nordlund, Å. 2006, A&A, 450, 1077
Braithwaite, J., & Spruit, H. C. 2004, Nature, 431, 819
Burleigh, M. R., Marsh, T. R., Gänsicke, B. T., et al. 2006, MNRAS, 373, 1416
Debes, J. H., López-Morales, M., Bonanos, A. Z., & Weinberger, A. J. 2006, ApJ, 647, L147
Donati, J. F., Achilleos, N., Matthews, J. M., & Wesemael, F. 1994, A&A, 285, 285
Euchner, F., Jordan, S., Beuermann, K., Gänsicke, B. T., & Hessman, F. V. 2002, A&A, 390, 633
Euchner, F., Reinsch, K., Jordan, S., Beuermann, K., & Gänsicke, B. T. 2005, A&A, 442, 651
Euchner, F., Jordan, S., Beuermann, K., Reinsch, K., & Gänsicke, B. T. 2006, A&A, 451, 671
Farihi, J., Burleigh, M. R., & Hoard, D. W. 2008, ApJ, 674, 421
Friedrich, S., Ostreicher, R., Ruder, H., & Zeller, G. 1994, A&A, 282, 179
Fukugita, M., Ichikawa, T., Gunn, J. E., et al. 1996, AJ, 111, 1748
Gänsicke, B. T., Schmidt, G. D., Jordan, S., & Szkody, P. 2001, ApJ, 555, 380
Gänsicke, B. T., Euchner, F., & Jordan, S. 2002, A&A, 394, 957
Harris, H. C., Liebert, J., Kleinman, S. J., et al. 2003, AJ, 126, 1023
Holberg, J. B., & Bergeron, P. 2006, AJ, 132, 1221
Jordan, S. 1992, A&A, 265, 570
Jordan, S. 2001, in 12th European Workshop on White Dwarfs, ed. J. L. Provencal, H. L. Shipman, J. MacDonald, & S. Goodchild, ASP Conf. Ser., 226, 269
Jordan, S. 2009, ArXiv e-prints
Jordan, S., & Schmidt, H. 2003, in Stellar Atmosphere Modeling, ed. I. Hubeny, D. Mihalas, & K. Werner, ASP Conf. Ser., 288, 625
Kawka, A., Vennes, S., Schmidt, G. D., Wickramasinghe, D. T., & Koch, R. 2007, ApJ, 654, 499
Kleinman, S. J., Harris, H. C., Eisenstein, D. J., et al. 2004, ApJ, 607, 426
Landolfi, M., Bagnulo, S., & Landi degl'Innocenti, M. 1998, A&A, 338, 111
Latter, W. B., Schmidt, G. D., & Green, R. F. 1987, ApJ, 320, 308
Liebert, J., Bergeron, P., Schmidt, G. D., & Saffer, R. A. 1993, ApJ, 418, 426
Liebert, J., Bergeron, P., & Holberg, J. B. 2003, AJ, 125, 348
Muslimov, A. G., van Horn, H. M., & Wood, M. A. 1995, ApJ, 442, 758
Putney, A. 1995, ApJ, 451, L67
Rechenberg, I. 1994, Werkstatt Bionik und Evolutionstechnik No. 1 (Stuttgart: frommann-holzboog
Reimers, D., Jordan, S., Beckmann, V., Christlieb, N., & Wisotzki, L. 1998, A&A, 337, L13
Schmidt, G. D., West, S. C., Liebert, J., Green, R. F., & Stockman, H. S. 1986, ApJ, 309, 218
Schmidt, G. D., Vennes, S., Wickramasinghe, D. T., & Ferrario, L. 2001, MNRAS, 328, 203
Schmidt, G. D., Harris, H. C., Liebert, J., et al. 2003, ApJ, 595, 1101
Schmidt, G. D., Szkody, P., Silvestri, N. M., et al. 2005, ApJ, 630, L173
Shorlin, S. L. S., Wade, G. A., Donati, J.-F., et al. 2002, A&A, 392, 637
Stoughton, C., Lupton, R. H., Bernardi, M., et al. 2002, AJ, 123, 485
Tillich, A., Geier, S., Heber, U., et al. 2009, [arXiv:0901.1030]
Tout, C. A., Wickramasinghe, D. T., Liebert, J., Ferrario, L., & Pringle, J. E. 2008, MNRAS, 387, 897
Vanlandingham, K. M., Schmidt, G. D., Eisenstein, D. J., et al. 2005, AJ, 130, 734
Wickramasinghe, D. T., & Ferrario, L. 2000, PASP, 112, 873
Wickramasinghe, D. T., & Ferrario, L. 2005, MNRAS, 356, 1576
Zhang, E.-H., Robinson, E. L., & Nather, R. E. 1986, ApJ, 305, 740

**Table 3.** Model fits with centered dipole and offset dipole models with comparison to literature values. The columns indicate the SDSS name of the object; the plate, Modified Julian Date and fiber ids of the observations; the dipole magnetic field strength of the centered dipole, the inclination with respect to the line of sight of the centered dipole, the dipole magnetic field strength of the offset dipole, the inclination with respect to the line of sight of the offset dipole, the offset along the axis of the magnetic field in terms of the stellar radius, and finally comments indicate the model parameters from the literature (i.e. Gänsicke et al. 2002; Schmidt et al. 2003; Vanlandingham et al. 2005)

| MWD (SDSS+) | Plate-MJD-FiberID | $B_p$/MG | $i$/deg | $B_{off}$/MG | $z_{off}/r_{WD}$ | $i$/deg | fits |
|---|---|---|---|---|---|---|---|
| J002129.00+150223.7 | 753-52233-432 | 530.69 ± 63.56 | 53.19 ± 25.64 | 527.33 ± 97.98 | 0.16 ± 0.08 | 28.05 ± 51.8 | 550 MG, ... |
| J004248.19+001955.3 | 690-52261-594 | 2.00 ± 0.00[2] | 88.22 ± 43.37 | 2.58[1] | 0.35 ± 0.82 | 0.00 ± 23.66 | 14 MG, 30° |
| J021116.34+003128.5 | 405-51816-382 | 341.31 ± 54.34 | 37.73 ± 27.71 | 281.34 ± 186.95 | 0.32 ± 0.14 | 9.59 ± 62.99 | 490 MG, ... |
| J021148.22+211548.2 | 246-53327-048 | 166.16 ± 7.41 | 48.89 ± 5.67 | 180.47 ± 13.15 | 0.27 ± 0.02 | 33.23 ± 10.05 | 210 MG, 90° |
| J023420.63+264801.7 | 2399-53764-559 | 32.82 ± 6.26 | 42.08 ± 8.09 | 21.17 ± 2.02 | 0.38 ± 0.04 | 17.17 ± 10.92 | |
| J030407.40-002541.7 | 411-51817-172 | 10.95 ± 0.98 | 48.57 ± 5.72 | 11.13 ± 0.97 | 0.27 ± 0.10 | 51.51 ± 17.26 | 11 MG, 60° |
| J031824.19+422651.0 | 2417-53766-568 | 10.12 ± 0.10 | 54.6 ± 4.7 | 10.77 ± 0.10 | 0.29 ± 0.05 | 61.1 ± 10.0 | |
| J032628.17+052136.3 | 2339-53729-515 | 16.87 ± 2.41 | 53.06 ± 26.65 | 17.49 ± 8.32 | 0.34 ± 0.12 | 44.62 ± 42.63 | |
| J033145.69+004517.0 | 415-51879-378 | 13.13 ± 1.00 | 49.41 ± 38.17 | 12.12 ± 9.98 | 0.21 ± 0.02 | 47.43 ± 38.49 | 12 MG, 60° |
| J033320.36+000720.6 | 0415-51879-485 | 849.30 ± 51.75 | 50.92 ± 8.75 | 784.22 ± 83.98 | 0.19 ± 0.05 | 6.29 ± 6.42 | |
| J034308.18-064127.3 | 462-51909-117 | 9.96 ± 2.06 | 41.96 ± 9.80 | 9.18 ± 2.11 | 0.23 ± 0.04 | 12.59 ± 8.55 | 13 MG, 45 |
| J034511.11+003444.3 | 416-51811-590 | 1.96 ± 0.42 | 49.01 ± 11.56 | 1.46 ± 0.36 | 0.34 ± 0.08 | 16.38 ± 6.43 | 1.5 MG, 0° |
| J074850.48+301944.8 | 889-52663-507 | 6.75 ± 0.41 | 40.65 ± 7.59 | 8.03 ± 0.66 | 0.40 ± 0.14 | 43.85 ± 10.55 | 10 MG, 60° |
| J074924.91+171355.4 | 2729-54419-282 | 13.99 ± 1.30 | 46.00 ± 15.07 | 13.62 ± 1.86 | 0.27 ± 0.05 | 44.02 ± 53.16 | |
| J075234.96+172525.0 | 1920-53314-106 | 10.30 ± 1.23 | 72.4 ± 22.4 | 11.73 ± 1.05 | 0.26 ± 0.05 | 58.7 ± 38.1 | |
| J075819.57+354443.7 | 757-52238-144 | 26.40 ± 3.94 | 37.62 ± 22.98 | 32.42 ± 5.65 | 0.39 ± 0.07 | 54.51 ± 19.44 | 27 MG, 30° |
| J080359.93+122944.0 | 2265-53674-033 | 40.7 ± 2.13 | 42.97 ± 8.44 | 26.6 ± 11.8 | 0.26 ± 0.04 | 17.71 ± 7.21 | |
| J080440.35+182731.0 | 2081-53357-442 | 48.47 ± 2.93 | 35.67 ± 7.59 | 29.26 ± 3.18 | 0.16 ± 0.02 | 33.97 ± 8.47 | 49 MG, 30° |
| J080502.29+215320.5 | 1584-52943-132 | 6.11 ± 1.29 | 54.76 ± 14.52 | 3.13 ± 0.59 | 0.39 ± 0.06 | 86.79 ± 59.37 | 5 MG, 60° |
| J080743.33+393829.2 | 545-52202-009 | 65.75 ± 18.52 | 78.07 ± 35.46 | 64.74 ± 12.14 | −0.01 ± 0.01 | 8.25 ± 17.26 | 49 MG, 30° |
| J080938.10+373053.8 | 758-52253-044 | 39.74 ± 5.41 | 41.89 ± 14.11 | 30.60 ± 5.66 | 0.20 ± 0.10 | 15.15 ± 75.23 | 40 MG, 30° |
| J081648.71+041223.5 | 1184-52641-329 | 10.13 ± 8.03 | 48.82 ± 29.96 | 6.50 ± 2.73 | 0.31 ± 0.12 | 0.28 ± 27.06 | 10* MG, 30*° |
| J081716.39+200834.8 | 2082-53358-444 | 3.37 ± 0.44 | 49.02 ± 10.78 | 3.37 ± 1.09 | 0.39 ± 0.10 | 34.05 ± 30.78 | |
| J082835.82+293448.7 | 1207-52672-635 | 33.40 ± 10.53 | 68.57 ± 33.47 | 34.60 ± 6.91 | 0.17 ± 0.05 | 50.3 ± 36.21 | 30 MG, 90*° |
| J083448.63+821059.1 | 2549 54523 135 | 14.44 ± 4.57 | 54.30 ± 66.45 | 14.36 ± 4.08 | 0.28 ± 0.09 | 48.58 ± 70.00 | |
| J083945.56+200015.7 | 2277-53705-484 | 3.38 ± 0.49 | 48.6 ± 7.7 | 2.15 ± 0.10 | 0.29 ± 0.08 | 49.9 ± 90[1] | |
| J084155.74+022350.6 | 564-52224-248 | 5.00 ± 0.99 | 49.35 ± 17.53 | 2.94 ± 0.72 | 0.16 ± 0.04 | 15.89 ± 10.57 | 6 MG, 90° |
| J085106.12+120157.8 | 2430-53815-229 | 2.03 ± 0.10 | 81.9 ± 90[1] | 2.47 ± 0.10 | 0.35 ± 0.06 | 72.8 ± 18.8 | |
| J085523.87+164059.0 | 2431-53818-522 | 12.23 ± 2.92 | 48.6 ± 8.6 | 7.86 ± 1.63 | 0.36 ± 0.06 | 10.8 ± 6.1 | |
| J085550.67+824905.3 | 2549 54523 066 | 10.82 ± 2.99 | 54.81 ± 19.36 | 12.13 ± 4.30 | 62.89 ± 36.38 | 0.30 ± 0.14 | |
| J085830.85+412635.1 | 830-52293-070 | 3.38 ± 0.19 | 48.85 ± 5.86 | 2.15 ± 0.34 | 0.24 ± 0.07 | 36.25 ± 7.31 | 2 MG, 30° |
| J090632.66+080716.0 | 1300-52973-148 | 5.98 ± 3.02 | 88.00 ± 88.06 | 5.97 ± 3.13 | 0.18 ± 0.13 | 65.13 ± 82.65 | 10 MG, 90° |
| J090746.84+353821.5 | 1212-52703-187 | 22.40 ± 8.80 | 48.57 ± 16.68 | 11.91 ± 3.22 | 0.26 ± 0.08 | 1.77 ± 2.72 | 15 MG, 60° |
| J091005.44+081512.2 | 1300-52973-639 | 1.01 ± 0.00[2] | 74.46 ± 42.54 | 1.27 ± 0.70 | 71.06 ± 32.03 | 0.35 ± 0.29 | |
| J091124.68+420255.9 | 1200-52668-538 | 35.20 ± 5.83 | 35.1 ± 39.48 | 18.85 ± 4.86 | 0.23 ± 0.06 | 14.23 ± 10.72 | 45 MG, 60° |
| J091437.40+054453.3 | 1193-52652-481 | 9.16 ± 0.77 | 48.52 ± 4.56 | 8.93 ± 0.93 | 0.38 ± 0.04 | 48.35 ± 19.7 | 9.5 MG, 90° |
| J091833.32+205536.9 | 2288-53699-547 | 2.04 ± 0.10 | 87.2 ± 41.9 | 2.66 ± 1.71 | 0.39 ± 0.17 | 70.3 ± 61.9 | |
| J092527.47+011328.7 | 475-51965-315 | 2.04 ± 0.00[2] | 54.83 ± 14.14 | 3.14 ± 1.10 | 0.33 ± 0.13 | 47.34 ± 14.08 | 2.2 MG, ... |
| J093356.40+102215.7 | 1303-53050-525 | 2.11 ± 0.49 | 72.05 ± 22.68 | 2.47 ± 0.00[2] | 0.37 ± 0.12 | 52.39 ± 29.38 | 1.5 MG, 60*° |
| J093409.90+392759.3 | 1215-52725-241 | 1.01 ± 0.00[2] | 81.18 ± 23.30 | 1.35 ± 0.25 | 57.43 ± 29.65 | 0.39 ± 0.13 | |
| J093447.90+503312.2 | 901-52641-373 | 7.35 ± 2.21 | 54.61 ± 37.93 | 4.29 ± 1.06 | 0.28 ± 0.07 | 46.87 ± 49.83 | 9.5 MG, 60° |

**Table 3.** continued.

| MWD (SDSS+) | Plate-MJD-FiberID | $B_p$/MG | $i$ / deg | $B_{off}$/MG | $z_{off}/r_{WD}$ | $i$ / deg | Comments |
|---|---|---|---|---|---|---|---|
| J094235.02+205208.3 | 2292-53713-019 | 39.21 ± 4.55 | 3.73 ± 1.64 | 37.94 ± 9.07 | 0.04 ± 0.02 | 1.24 ± 13.74 | |
| J094458.92+453901.2 | 1202-52672-577 | 15.91 ± 9.10 | 68.35 ± 44.53 | 17.41 ± 7.12 | 0.34 ± 0.14 | 61.00 ± 90[1] | 14 MG, 90° |
| J100005.67+015859.2 | 500-51994-557 | 19.74 ± 10.26 | 48.5 ± 33.13 | 8.10 ± 3.23 | 0.34 ± 0.13 | 4.21 ± 90[1] | 20 MG, 30° |
| J100356.32+053825.6 | 996-52641-295 | 672.07 ± 118.63 | 40.8 ± 34.86 | 667.67 ± 131.71 | 0.08 ± 0.05 | 36.67 ± 23.11 | 900* MG, ... |
| J100657.51+303338.1 | 1953-53358-415 | 1.00 ± 0.10 | 82.5 ± 30.8 | 1.30 ± 1.23 | −0.37 ± 0.39 | 14.3 ± 13.1 | |
| J100715.55+123709.5 | 1745-53061-313 | 5.41 ± 67.28 | 68.6 ± 31.88 | 6.01 ± 2.55 | 0.40 ± 0.22 | 50.7 ± 90[1] | 7 MG, 60° |
| J100759.80+162349.6 | 2585 54097 030 | 19.18 ± 3.36 | 42.02 ± 17.48 | 13.50 ± 2.92 | −0.22 ± 0.05 | 33.31 ± 21.38 | |
| J101428.09+365724.3 | 1954-53357-393 | 11.09 ± 1.50 | 48.75 ± 11.72 | 12.14 ± 2.71 | 0.05 ± 0.04 | 56.81 ± 34.40 | |
| J101529.62+090703.8 | 1237-52762-533 | 4.09 ± 0.86 | 49 ± 15.27 | 1.98 ± 0.35 | 0.26 ± 0.08 | 1.48 ± 60.69 | 5* MG, 90*° |
| J101618.37+040920.6 | 574-52355-166 | 2.01 ± 0.00[2] | 88.16 ± 104.01 | 7.24 ± 4.77 | 0.19 ± 0.16 | 60.55 ± 63.4 | 7.5 MG, 30° |
| J101805.04+011123.5 | 503-51999-244 | 99.92 ± 5.90 | 27.24 ± 6.16 | 39.87 ± 2.25 | 0.26 ± 0.02 | 14.85 ± 3.17 | 120 MG, ... |
| J102220.69+272539.8 | 2350-53765-543 | 4.91 ± 0.31 | 27.58 ± 30.65 | 5.79 ± 2.82 | 0.39 ± 0.27 | 54.97 ± 35.63 | |
| J102239.06+194904.3 | 2374-53765-544 | 2.94 ± 0.71 | 49.0 ± 13.0 | 3.87 ± 1.11 | 0.40 ± 0.07 | 51.3 ± 40.3 | |
| J103532.53+212603.5 | 2376-53770-534 | 2.96 ± 0.33 | 49.01 ± 9.51 | 1.515 ± 0.313 | 0.39 ± 0.05 | 0.00 ± 57.44 | |
| J105404.38+593333.3 | 561-52295-008 | 17.41 ± 7.90 | 90.0 ± 25.54 | 17.60 ± 10.22 | 0.16 ± 0.05 | 67.59 ± 59.48 | 17 MG, 90° |
| J105628.49+652313.5 | 490-51929-205 | 29.27 ± 5.78 | 41.74 ± 15.24 | 20.80 ± 4.10 | 0.29 ± 0.54 | 5.27 ± 12.8 | 28 MG, 60° |
| J105709.81+041130.3 | 580-52368-274 | 2.03 ± 0.00[2] | 48.99 ± 7.70 | 2.48 ± 0.0 | 41.40 ± 13.13 | 0.38 ± 0.06 | |
| J111010.50+600141.4 | 950-52378-568 | 6.37 ± 2.32 | 68.6 ± 16.26 | 6.71 ± 1.58 | 0.39 ± 0.08 | 49.08 ± 18.99 | 6.5 MG, 70° |
| J111812.67+095241.3 | 1222-52763-477 | 3.38 ± 0.72 | 48.14 ± 32.44 | 2.67 ± 0.60 | 0.40 ± 0.10 | 51.09 ± 43.5 | 6 MG, 60*° |
| J112030.34-115051.1 | 2874-54561-512 | 8.90 ± 1.02 | 50.37 ± 20.24 | 7.72 ± 1.24 | 0.35 ± 0.10 | 38.69 ± 34.08 | |
| J112257.10+322327.8 | 1979-53431-512 | 11.38 ± 3.42 | 49.0 ± 12.3 | 7.46 ± 1.68 | 0.37 ± 0.11 | 4.2 ± 6.3 | |
| J112328.49+095619.3 | 1222-52763-625 | 1.21 ± [2] | 81.18 ± 17.28 | 1.50 ± 0.36 | 0.39 ± 0.06 | 50.93 ± 90[1] | |
| J112852.88-010540.8 | 326-52375-565 | 2.00 ± 0.00[2] | 89.4 ± 85.15 | 2.30 ± 5.02 | 0.20 ± 0.14 | 23.15 ± 30.18 | 3 MG, 60° |
| J112926.23+493931.8 | 966-52642-474 | 5.31 ± 0.64 | 48.72 ± 6.34 | 2.43 ± 0.33 | 0.39 ± 0.09 | 7.04 ± 12.45 | 5 MG, 60° |
| J113215.38+280934.3 | 2219-53816-329 | 3.01 ± 0.82 | 49.00 ± 17.43 | 2.84 ± 0.43 | 0.39 ± 0.049 | 18.60 ± 5.56 | |
| J113357.66+515204.8 | 879-52365-586 | 8.64 ± 0.78 | 74.55 ± 19.87 | 7.69 ± 0.69 | 0.39 ± 0.04 | 47.91 ± 19.99 | 7.5 MG, 90° |
| J113756.50+574022.4 | 1311-52765-421 | 5.00 ± 0.34 | 33.45 ± 9.92 | 2.83 ± 0.25 | 0.17 ± 0.01 | 0.07 ± 0.06 | 9 MG, 60*° |
| J113839.51-014903.0 | 327-52294-583 | 22.71 ± 1.26 | 54.31 ± 14.41 | 24.09 ± 1.92 | 0.21 ± 0.04 | 50.16 ± 61.4 | 24 MG, 60° |
| J114006.37+611008.2 | 776-52319-042 | 50.19 ± 17.78 | 21.8 ± 42.46 | 52.82 ± 8.82 | 0.04 ± 0.02 | 36.88 ± 50.59 | 58 MG, 20° |
| J114829.00+482731.2 | 1446-53080-324 | 32.47 ± 7.11 | 80.89 ± 45.93 | 32.44 ± 2.70 | 0.17 ± 0.09 | 69.98 ± 33.06 | 33 MG, 90° |
| J115418.14+011711.4 | 515-52051-126 | 33.47 ± 2.07 | 88.14 ± 23.62 | 25.72 ± 2.51 | 0.10 ± 0.03 | 76.03 ± 32.13 | 32 MG, 45 |
| J115917.39+613914.3 | 777-52320-69 | 20.10 ± 6.70 | 50.63 ± 62.9 | 10.14 ± 6.89 | 0.30 ± 0.07 | 50.63 ± 62.9 | 15.5 MG, 60° |
| J120150.10+614257.0 | 778-52337-264 | 11.35 ± 1.53 | 28.04 ± 10.98 | 7.60 ± 0.87 | 0.16 ± 0.02 | 18.59 ± 12.62 | 20 MG, 90° |
| J120609.80+081323.7 | 1623-53089-573 | 760.63 ± 281.66 | 30.74 ± 36.38 | 312.24 ± 73.90 | 0.24 ± 0.13 | 25.69 ± 24.66 | 830* MG, ... |
| J120728.96+440731.6 | 1369-53089-048 | 2.03 ± 0.00[2] | 73.01 ± 29.93 | 2.07 ± 0.00[2] | −0.27 ± 0.59 | 10.16 ± 21.53 | 2.5 MG, 90° |
| J121209.31+013627.7 | 518-52282-285 | 10.12 ± 0.93 | 48.8 ± 4.69 | 10.38 ± 1.02 | 0.29 ± 0.05 | 40.65 ± 13.27 | 13 MG, 80° |
| J121635.37-002656.2 | 288-52000-276 | 59.70 ± 10.23 | 37.85 ± 37.52 | 44.57 ± 7.18 | −0.06 ± 0.01 | 20.15 ± 30.89 | 61 MG, 90° |
| J122209.44+001534.0 | 289-51990-349 | 14.70 ± 4.70 | 82.52 ± 90[1] | 16.27 ± 11.39 | 0.24 ± 0.31 | 82.52 ± 90[1] | 14 MG, 80° |
| J122249.14+481133.1 | 1451-53117-582 | 8.05 ± 2.24 | 56.67 ± 13.05 | 8.70 ± 3.90 | −0.38 ± 0.08 | 53.05 ± 18.28 | 8 MG, 90*° |
| J122401.48+415551.9 | 1452-53112-181 | 22.36 ± 3.02 | 66.08 ± 23.71 | 24.75 ± 5.76 | 0.26 ± 0.06 | 58.28 ± 23.89 | 23* MG, 60° |
| J123414.11+124829.6 | 1616-53169-423 | 4.32 ± 0.27 | 49.35 ± 9.82 | 2.40 ± 0.56 | 0.40 ± 0.05 | 9.99 ± 2.72 | 7 MG, 60*° |
| J124806.38+410427.2 | 1456-53115-190 | 7.03 ± 1.19 | 48.81 ± 9.27 | 3.61 ± 0.47 | 0.29 ± 0.06 | 5.5 ± 10.08 | 8 MG, 90° |
| J124836.31+294231.2 | 2457-54180-112 | 3.95 ± 0.25 | 48.93 ± 4.93 | – | – | – | |
| J124851.31-022924.7 | 337-51997-264 | 7.36 ± 2.19 | 48.9 ± 10.11 | 8.01 ± 1.46 | 0.40 ± 0.09 | 49.97 ± 27.39 | 7 MG, 40° |

**Table 3.** continued.

| MWD (SDSS+) | Plate-MJD-FiberID | $B_p$/MG | $i$ / deg | $B_{off}$/MG | $z_{off}/r_{WD}$ | $i$ / deg | Comments |
|---|---|---|---|---|---|---|---|
| J125044.42+154957.4 | 1770-53171-530 | 20.71 ± 3.66 | 56.7 ± 11.21 | 20.30 ± 2.43 | 0.12 ± 0.02 | 53.83 ± 38.18 | 20 MG, 60° |
| J125416.01+561204.7 | 1318-52781-299 | 38.86 ± 9.03 | 20.97 ± 40.41 | 36.98 ± 9.20 | 0.01 ± 1$e$ + 99 | 10.25 ± 21.24 | 52 MG, 30° |
| J125434.65+371000.1 | 1989-53772-041 | 4.10 ± 0.35 | 41.9 ± 19.2 | 4.89 ± 0.42 | 0.40 ± 0.03 | 50.1 ± 21.0 | |
| J125715.54+341439.3 | 2006-53476-332 | 11.45 ± 0.71 | 0.5 ± 0.6 | 13.70 ± 1.69 | 0.07 ± 0.02 | 7.7 ± 12.0 | |
| J132002.48+131901.6 | 1773-53112-011 | 2.02 ± 0.00[2] | 88.21 ± 80.46 | 2.64 ± 4.88 | −0.38 ± 0.52 | 6.99 ± 35.73 | 5 MG, 60° |
| J133340.34+640627.4 | 603-52056-112 | 10.71 ± 1.03 | 50.29 ± 11.45 | 13.81 ± 1.36 | 0.38 ± 0.07 | 55.7 ± 24.63 | 13 MG, 60° |
| J134043.10+654349.2 | 497-51989-182 | 4.32 ± 0.76 | 49.04 ± 9.75 | 5.28 ± 1.07 | 0.40 ± 0.06 | 34.03 ± 6.8 | 3 MG, 60° |
| J134820.79+381017.2 | 2014-53460-236 | 13.65 ± 2.66 | 89.4 ± 90[1] | 14.45 ± 4.65 | 0.22 ± 0.04 | 54.8 ± 25.3 | |
| J135141.13+541947.4 | 1323-52797-293 | 761.00 ± 56.42 | 74.18 ± 21.65 | 772.73 ± 94.41 | −0.03 ± 0.01 | 68.25 ± 62.04 | 760 MG, 20° |
| J140716.66+495613.7 | 1671-53446-453 | 12.49 ± 6.20 | 88.1 ± 90[1] | 13.20 ± 4.21 | 0.24 ± 0.10 | 63.3 ± 81.1 | |
| J141906.19+254356.5 | 2131-53819-317 | 2.03 ± 0.10 | 81.2 ± 8.7 | 2.56 ± 0.10 | 0.38 ± 0.03 | 54.8 ± 10.4 | |
| J142703.40+372110.5 | 1381-53089-182 | 27.04 ± 3.20 | 56.89 ± 12.61 | 30.59 ± 2.34 | 0.20 ± 0.02 | 6.39 ± 22.5 | 30 MG, 60*° |
| J143019.05+281100.8 | 2134-53876-423 | 9.34 ± 1.44 | 5.6 ± 4.5 | 6.25 ± 0.75 | 0.16 ± 0.03 | 5.6 ± 4.5 | |
| J143218.26+430126.7 | 1396-53112-338 | 1.01 ± 0.00[2] | 78.3 ± 90[1] | 1.48[1] | −0.39 ± 0.56 | 55.37 ± 81.19 | 1.5 MG, 90° |
| J143235.46+454852.5 | 1288-52731-449 | 12.29 ± 6.98 | 50.62 ± 88.7 | 13.08 ± 4.78 | 0.40 ± 0.11 | 25.84 ± 33.41 | 10 MG, 30° |
| J144614.00+590216.7 | 608-52081-140 | 4.42 ± 3.79 | 48.9 ± 31.58 | 2.18 ± 0.00[2] | 0.40 ± 0.26 | 4.72 ± 13.13 | 7 MG, 70° |
| J145415.01+432149.5 | 1290-52734-469 | 2.35 ± 0.88 | 49.04 ± 17.87 | 2.15 ± 1.09 | 0.27 ± 0.11 | 53.38 ± 22.89 | 5 MG, ... |
| J150813.20+394504.9 | 1398-53146-633 | 13.23 ± 3.11 | 37.55 ± 4.17 | 7.96 ± 0.76 | 0.40 ± 0.04 | 24.68 ± 5.61 | 20 MG, 90° |
| J151130.17+422023.0 | 1291-52735-612 | 22.40 ± 9.41 | 48.6 ± 19.5 | 8.37 ± 1.07 | 0.31 ± 0.06 | 5.8 ± 21.1 | 12 MG, 60° |
| J151415.65+074446.5 | 1817-53851-534 | 35.34 ± 2.80 | 56.59 ± 17.23 | 35.88 ± 3.75 | 0.12 ± 0.043 | 56.08 ± 22.18 | |
| J151745.19+610543.6 | 613-52345-446 | 13.98 ± 7.36 | 60.07 ± 196.18 | 6.07 ± 3.24 | 0.23 ± 0.35 | 24.86 ± 47.72 | 17 MG, 30° |
| J152401.60+185659.2 | 2794-54537-410 | 11.96 ± 1.85 | 41.53 ± 8.79 | 10.27 ± 3.12 | 0.11 ± 0.02 | 33.40 ± 6.58 | |
| J153532.25+421305.6 | 1052-52466-252 | 5.27 ± 4.05 | 0.35 ± 41.68 | 9.05 ± 5.27 | −0.29 ± 0.12 | 0.13 ± 0.37 | 4.5 MG, 60° |
| J153829.29+530604.6 | 795-52378-637 | 13.99 ± 3.82 | 48.96 ± 15.69 | 15.99 ± 3.03 | 0.36 ± 0.11 | 53.36 ± 29.05 | 12 MG, 30° |
| J153843.10+084238.2 | 1725 54266 297 | 13.20 ± 4.34 | 41.09 ± 90[1] | 9.63± | 24.98 ± 34.53 | 0.33 ± 0.08 | |
| J154213.48+034800.4 | 594-52045-400 | 8.35 ± 2.60 | 54.34 ± 35.5 | 8.25 ± 2.72 | 0.19 ± 0.16 | 44.48 ± 30.63 | 8 MG, 60° |
| J154305.67+343223.6 | 1402-52872-145 | 4.09 ± 2.67 | 62.06 ± 158.24 | 4.02 ± 1.09 | 0.20 ± 0.06 | 62.67 ± 22.69 | |
| J160437.36+490809.2 | 622-52054-330 | 59.51 ± 4.64 | 40.83 ± 28.87 | 38.36 ± 3.61 | 0.14 ± 0.02 | 7.95 ± 10.24 | 53 MG, 0° |
| J164357.02+240201.3 | 1414-53135-191 | 2.00 ± 0.00[2] | 88.01 ± 56.93 | 2.41 ± 10.10 | −0.34 ± 0.99 | 18.54 ± 33.29 | 4 MG, 90° |
| J164703.24+370910.3 | 818-52395-026 | 2.10 ± 0.67 | 68.39 ± 18.11 | 2.15 ± 1.21 | 0.28 ± 0.10 | 72.53 ± 18.41 | 2* MG, 90*° |
| J165029.91+341125.5 | 1175-52791-482 | 3.38 ± 0.67 | 48.78 ± 13.64 | 3.92 ± 1.05 | 0.40 ± 0.12 | 57.74 ± 32.5 | 3* MG, 0*° |
| J165203.68+352815.8 | 820-52438-299 | 7.37 ± 2.92 | 48.98 ± 11.77 | 9.53 ± 3.53 | 0.40 ± 0.08 | 51.15 ± 30.36 | 9.5 MG, 60° |
| J165249.09+333444.9 | 1175-52791-095 | 5.07 ± 4.18 | 54.25 ± 28.04 | 5.82 ± 1.90 | 0.39 ± 0.11 | 49.85 ± 36.73 | |
| J170400.01+321328.7 | 976-52413-319 | 50.11 ± 25.08 | 54.87 ± 118.04 | 56.16 ± 8.84 | 0.27 ± 0.05 | 0.34 ± 53.88 | 5 MG, 90*° |
| J171556.29+600643.9 | 354-51792-318 | 2.03 ± 0.00[2] | 86.63 ± 31.39 | 2.03 ± 0.00[2] | −0.19 ± 0.09 | 60.85 ± 35.29 | 4.5 MG, 60° |
| J172045.37+561214.9 | 367-51997-461 | 19.79 ± 5.42 | 56.7 ± 21.33 | 9.72 ± 2.68 | 0.31 ± 0.18 | 0.85 ± 36.62 | 7 MG, 30° |
| J172329.14+540755.8 | 359-51821-415 | 32.85 ± 3.56 | 37.43 ± 26.52 | 28.86 ± 2.71 | 0.04 ± 0.03 | 25.4 ± 27.51 | 35 MG, 10° |
| J172932.48+563204.1 | 358-51818-239 | 27.26 ± 7.04 | 51.19 ± 67.41 | 27.17 ± 18.71 | 0.22 ± 0.10 | 41.74 ± 90[1] | 35 MG, ... |
| J202501.10+131025.6 | 2257-53612-167 | 10.10 ± 1.76 | 68.5 ± 9.1 | 10.72 ± 1.71 | 0.29 ± 0.04 | 53.7 ± 9.0 | |
| J204626.15-071037.0 | 635-52145-227 | 2.03 ± 0.00[2] | 49.33 ± 25.34 | 2.62 ± 0.53 | 0.40 ± 0.06 | 54.97 ± 17.54 | 2 MG, 60° |
| J205233.52-001610.7 | 982-52466-019 | 13.42 ± 3.73 | 68.57 ± 12.86 | 1.31 ± 0.23 | 0.130.03 | 56.97 ± 16.83 | 13 MG, 80° |
| J214900.87+004842.8 | 1107-52968-374 | 10.09 ± 4.71 | 46.97 ± 99.7 | 5.53 ± 2.90 | 0.22 ± 0.11 | 5.00 ± 9.13 | 10 MG, 60° |
| J214930.74-072812.0 | 644-52173-350 | 44.71 ± 1.92 | 67.27 ± 26.38 | 44.71 ± 2.80 | 0.06 ± 0.05 | 60.11 ± 16.52 | 42 MG, 30° |
| J215148.31+125525.5 | 733-52207-522 | 20.76 ± 1.39 | 68.3 ± 12.21 | 21.80 ± 3.09 | 0.12 ± 0.03 | 68.66 ± 19.04 | 21 MG, 90° |

**Table 3.** continued.

| MWD (SDSS+) | Plate-MJD-FiberID | $B_p$/MG | $i$ / deg | $B_{off}$/MG | $z_{off}/r_{WD}$ | $i$ / deg | Comments |
|---|---|---|---|---|---|---|---|
| J220435.05+0012 42.9 | 372-52173-626 | 1.02 ± 0.10 | 71.2 ± 90[1] | 2.50 ± 5.47 | −0.36 ± 0.69 | 3.1 ± 13.6 | |
| J221828.59-000012.2 | 374-51791-583 | 257.54 ± 48.71 | 17.68 ± 17.63 | 212.18 ± 34.78 | 0.06 ± 0.02 | 17.09 ± 27.01 | 225 MG, 30° |
| J224741.46+145638.8 | 740-52263-444 | 42.11 ± 2.83 | 53.02 ± 9.70 | 46.95 ± 4.30 | −0.17 ± 0.02 | 33.16 ± 9.84 | 560 MG, … |
| J225726.05+075541.7 | 2310-53710-420 | 16.17 ± 2.81 | 74.9 ± 16.1 | 17.39 ± 3.21 | 0.15 ± 0.05 | 78.5 ± 34.8 | |
| J231951.73+010909.3 | 382-51816-565 | 9.35 ± 31.50 | 48.98 ± 11.36 | 6.06 ± 1.24 | 0.40 ± 0.09 | 12.48 ± 50.66 | 1.5* MG, 90*° |
| J232248.22+003900.9 | 383-51818-421 | 21.40 ± 3.36 | 49.00 ± 15.42 | 21.65 ± 4.48 | 0.29 ± 0.07 | 44.174 ± 25.58 | 19 MG, 60° |
| J234605.44+385337.6 | 1883-53271-272 | 798.1 ± 163.6 | 2.50 ± 1.07 | 706.0 ± 238.9 | 0.12 ± 0.06 | 86.6 ± 15.4 | 1000* MG, … |
| J234623.69-102357.0 | 648-52559-142 | 9.17 ± 1.58 | 48.78 ± 9.62 | 2.25 ± 0.29 | 0.39 ± 0.07 | 8.42 ± 2.6 | 2.5 MG, 90*° |

Asterisks indicate field strengths or inclinations with uncertainties greater than 10% in Vanlandingham et al. (2005).
[1] The errors are very large.
[2] The errors are very small.

## Appendix A: Figures of all fits not shown in the printed version

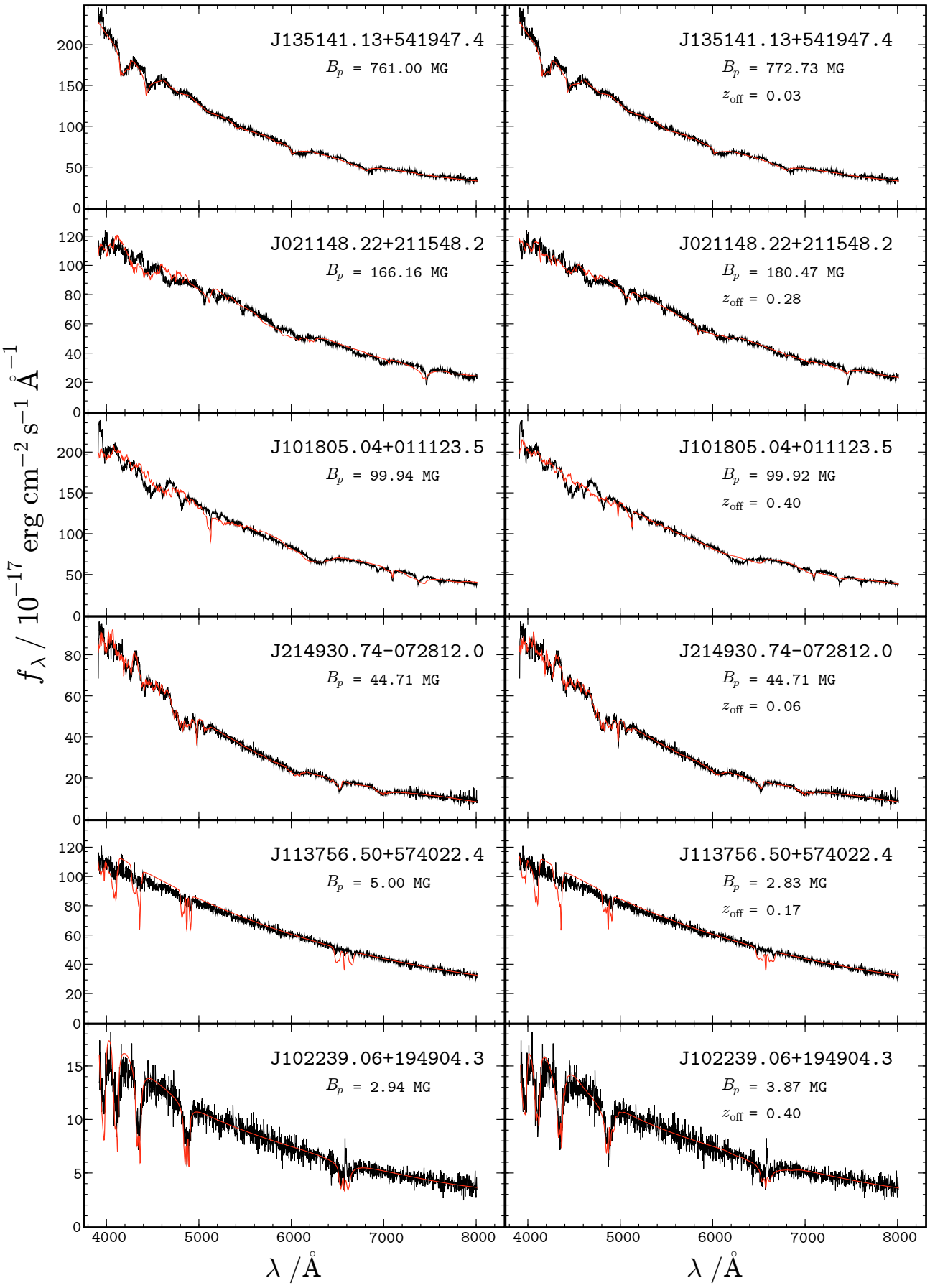


**Fig. A.1.** Color version of Fig. 1.

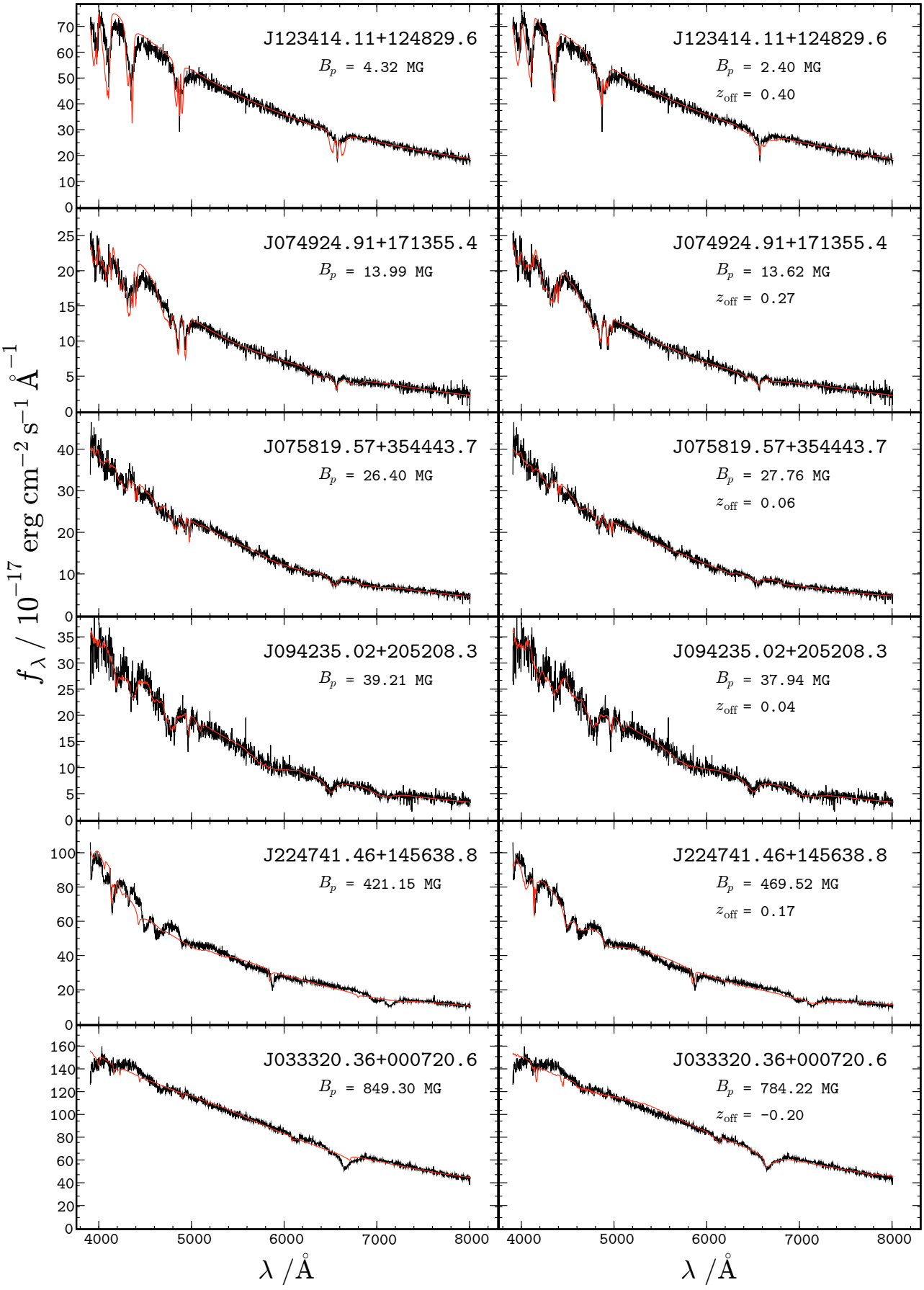


**Fig. A.2.** Color version of Fig. 2.

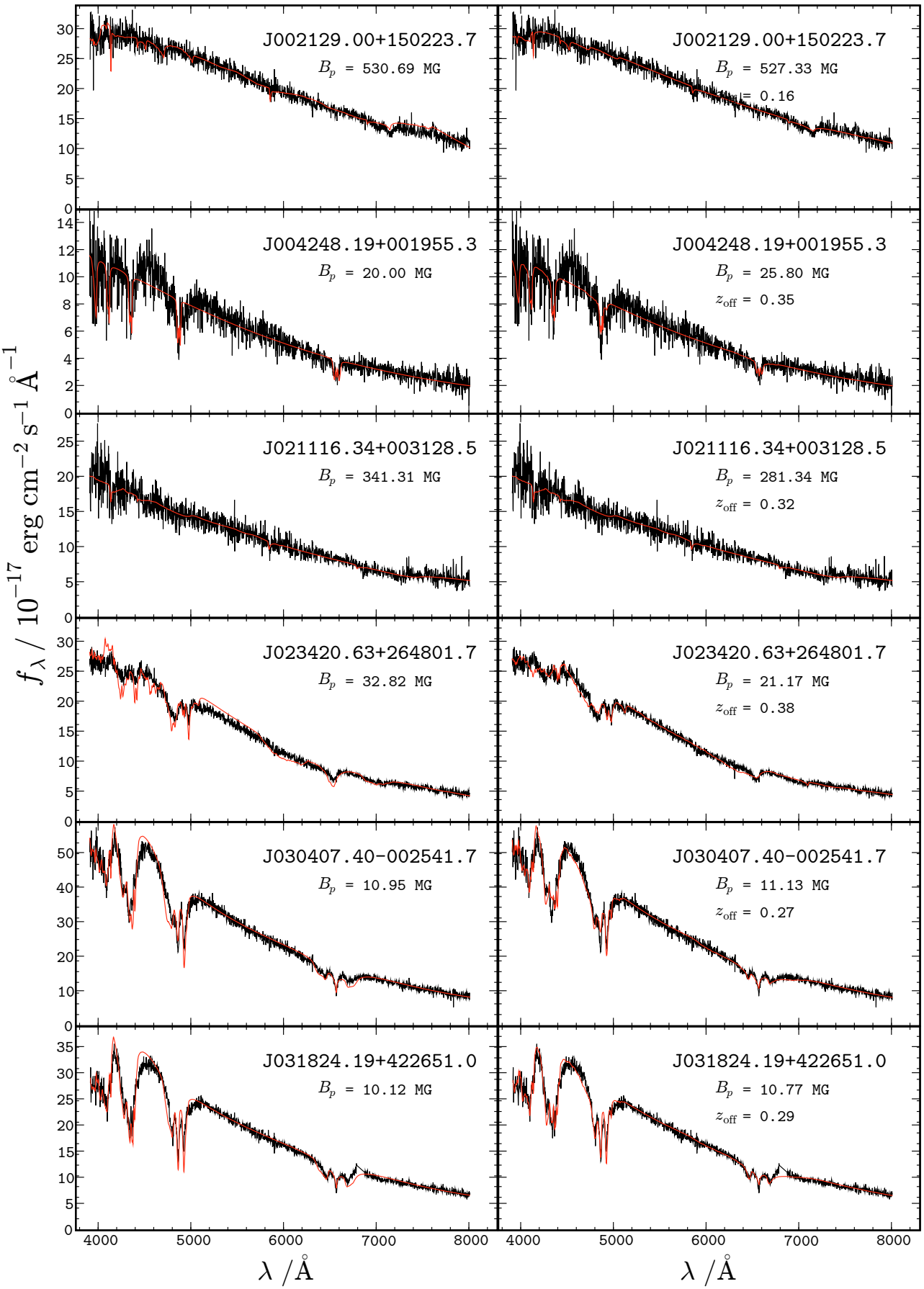


**Fig. A.3.** Fits of observed spectra of DAHs from the SDSS to centered magnetic dipoles with a polar field strength $B_{\rm p}$ (*left*) and dipoles shifted by $z_{\rm off}$ stellar radii along the dipole axis (*right*).

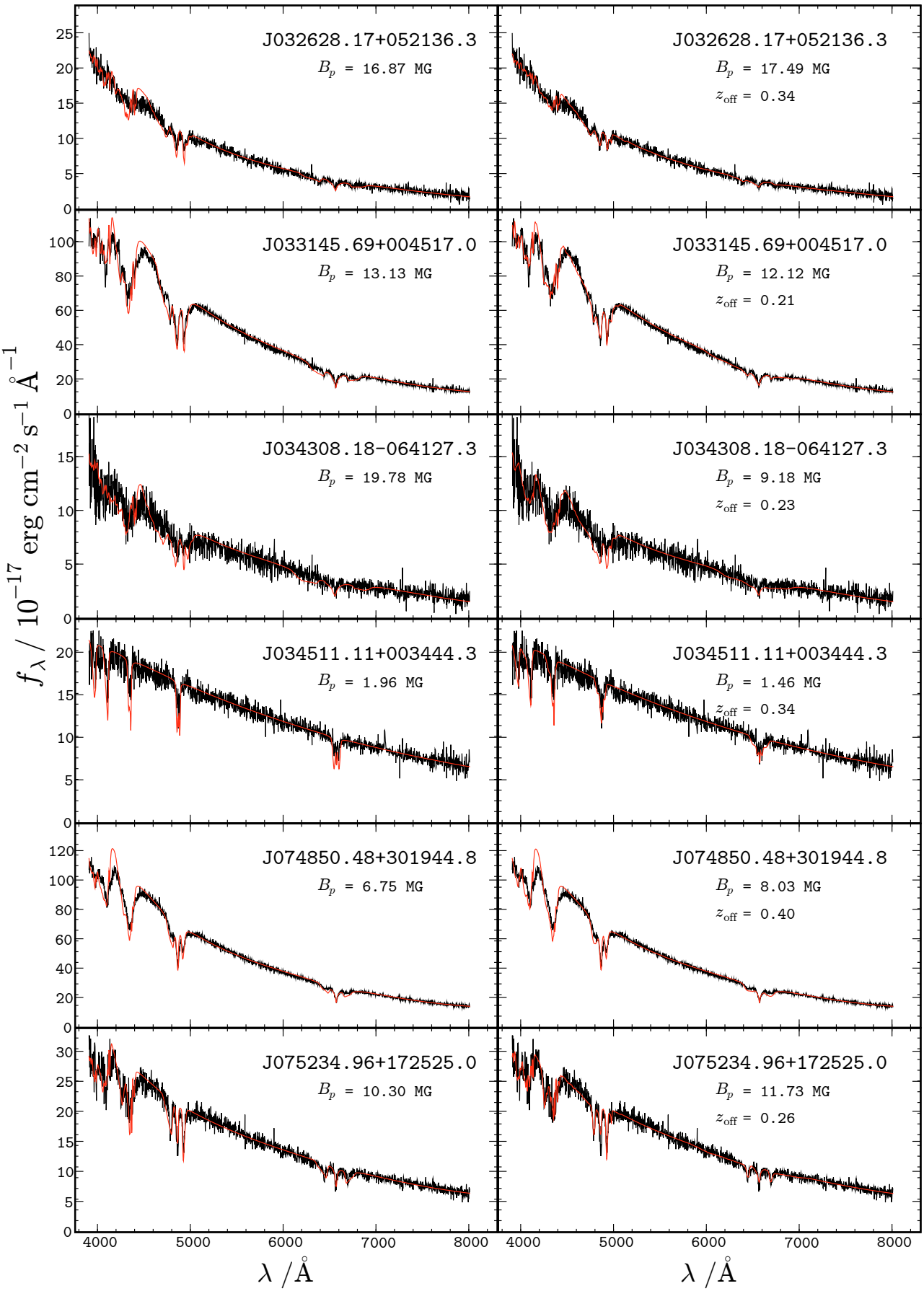


**Fig. A.4.** Fits of observed spectra of DAHs from the SDSS to centered magnetic dipoles with a polar field strength $B_{\rm p}$ (*left*) and dipoles shifted by $z_{\rm off}$ stellar radii along the dipole axis (*right*).

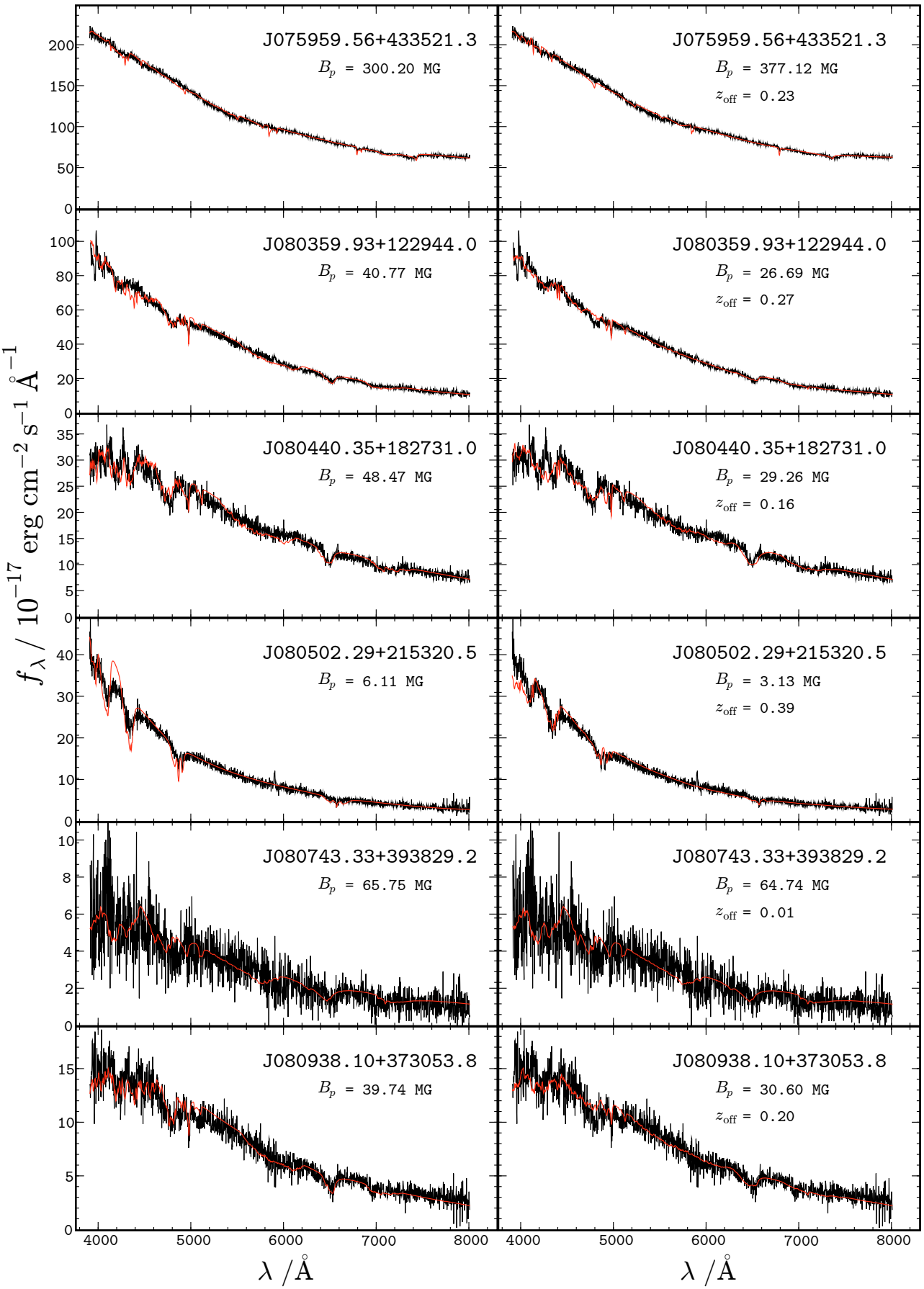


**Fig. A.5.** Fits of observed spectra of DAHs from the SDSS to centered magnetic dipoles with a polar field strength $B_{\rm p}$ (*left*) and dipoles shifted by $z_{\rm off}$ stellar radii along the dipole axis (*right*).

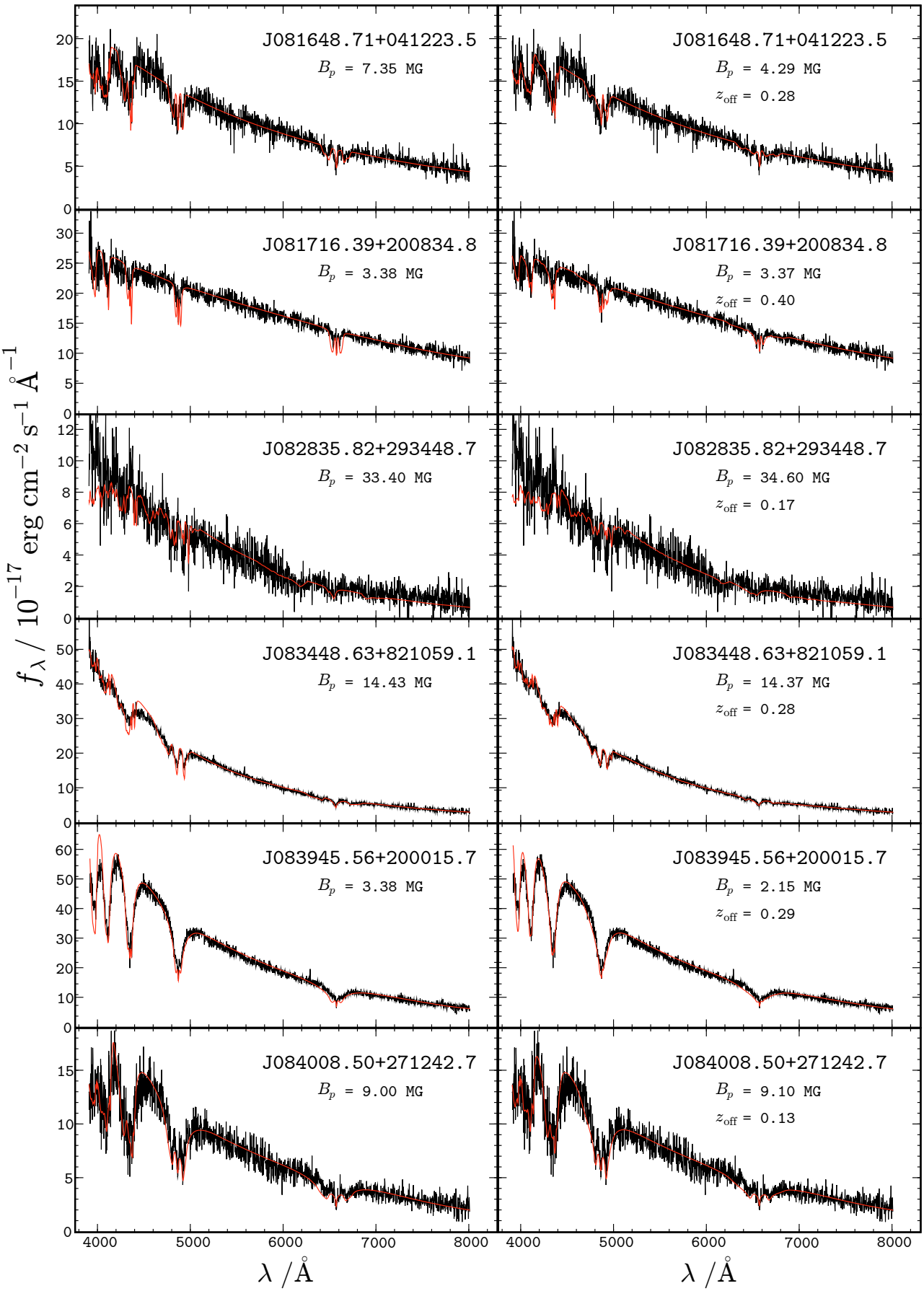


**Fig. A.6.** Fits of observed spectra of DAHs from the SDSS to centered magnetic dipoles with a polar field strength $B_{\rm p}$ (*left*) and dipoles shifted by $z_{\rm off}$ stellar radii along the dipole axis (*right*).

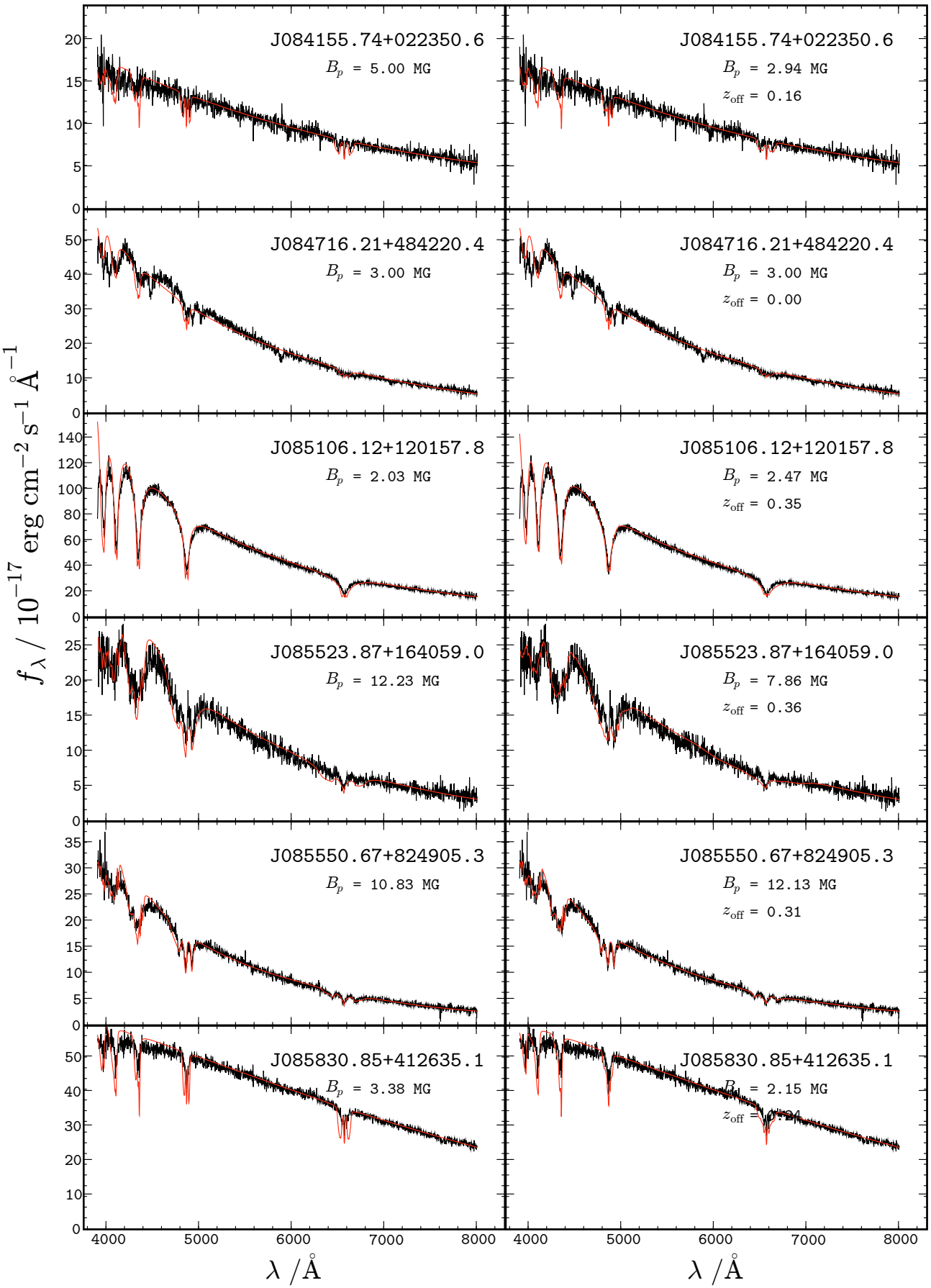


**Fig. A.7.** Fits of observed spectra of DAHs from the SDSS to centered magnetic dipoles with a polar field strength $B_{\rm p}$ (*left*) and dipoles shifted by $z_{\rm off}$ stellar radii along the dipole axis (*right*).

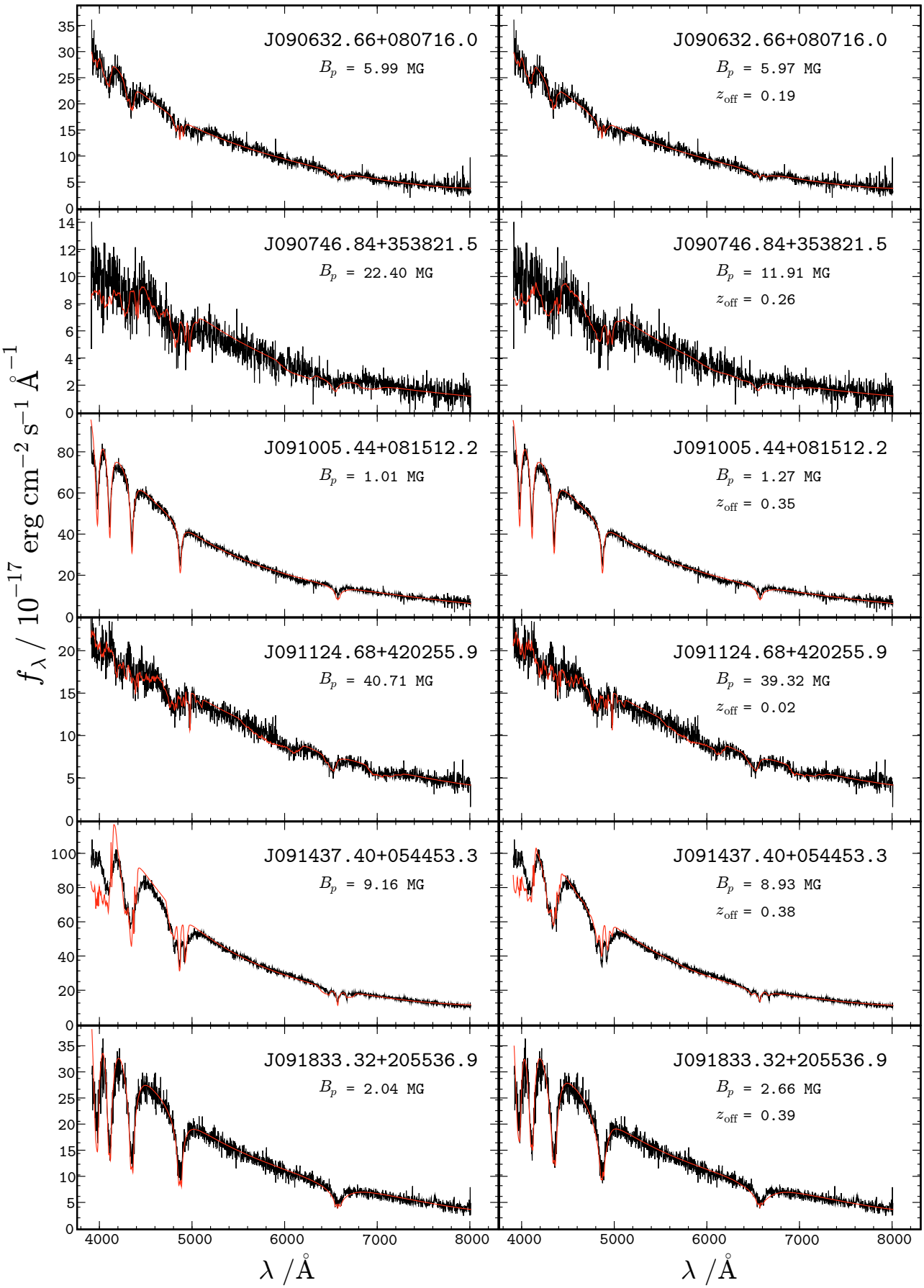


**Fig. A.8.** Fits of observed spectra of DAHs from the SDSS to centered magnetic dipoles with a polar field strength $B_{\rm p}$ (*left*) and dipoles shifted by $z_{\rm off}$ stellar radii along the dipole axis (*right*).

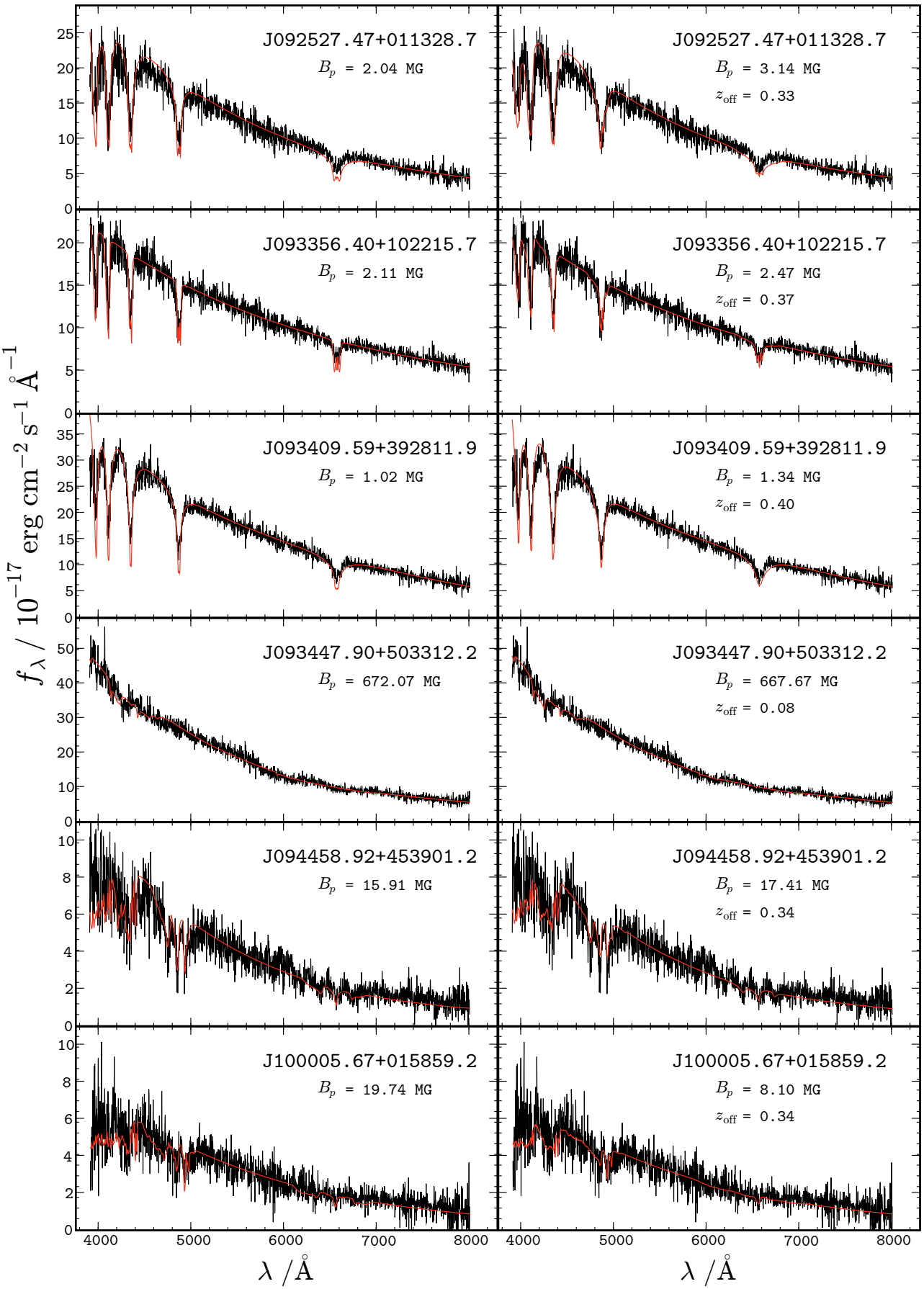


**Fig. A.9.** FFits of observed spectra of DAHs from the SDSS to centered magnetic dipoles with a polar field strength $B_{\rm p}$ (*left*) and dipoles shifted by $z_{\rm off}$ stellar radii along the dipole axis (*right*).

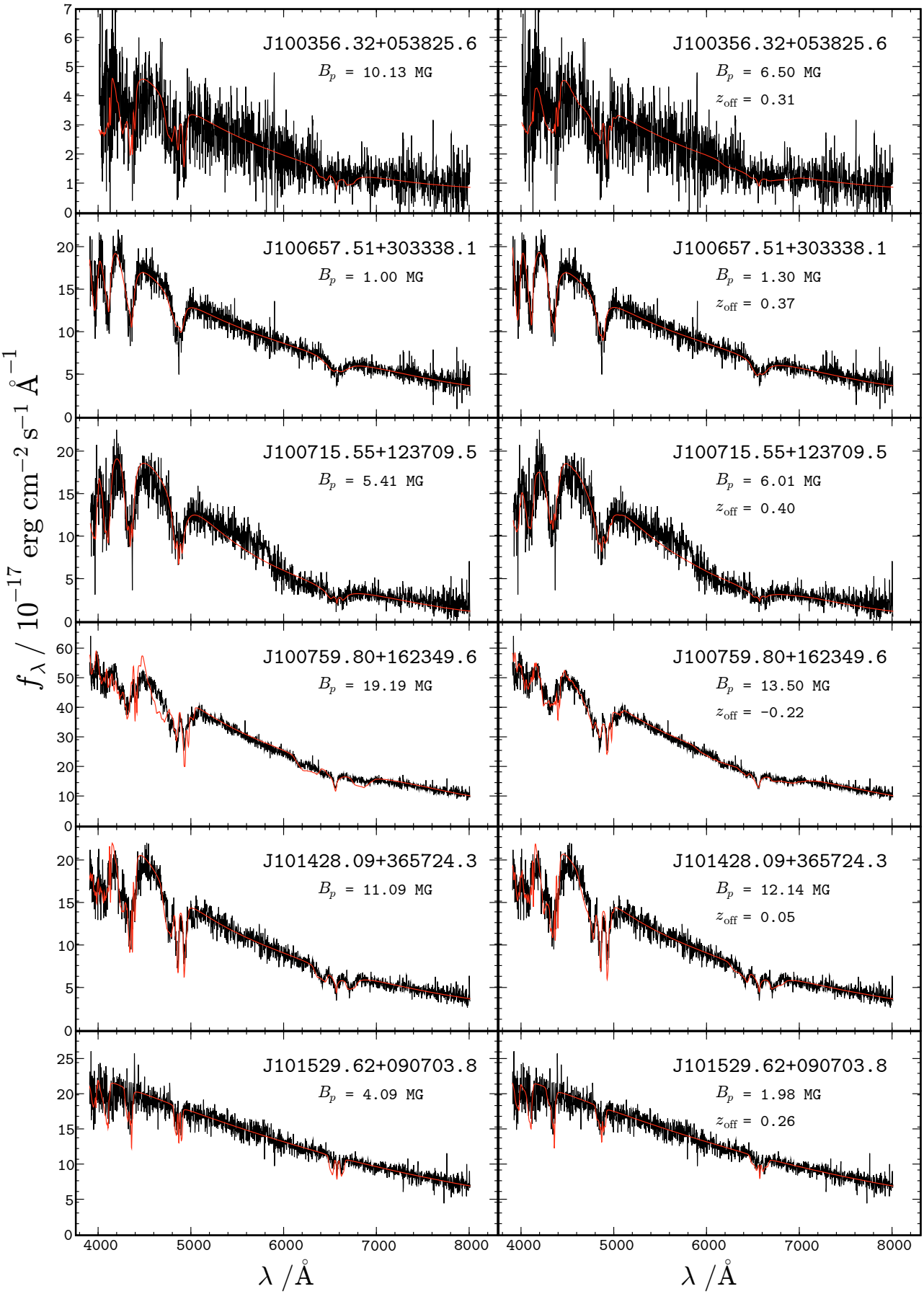


**Fig. A.10.** Fits of observed spectra of DAHs from the SDSS to centered magnetic dipoles with a polar field strength $B_{\rm p}$ (*left*) and dipoles shifted by $z_{\rm off}$ stellar radii along the dipole axis (*right*).

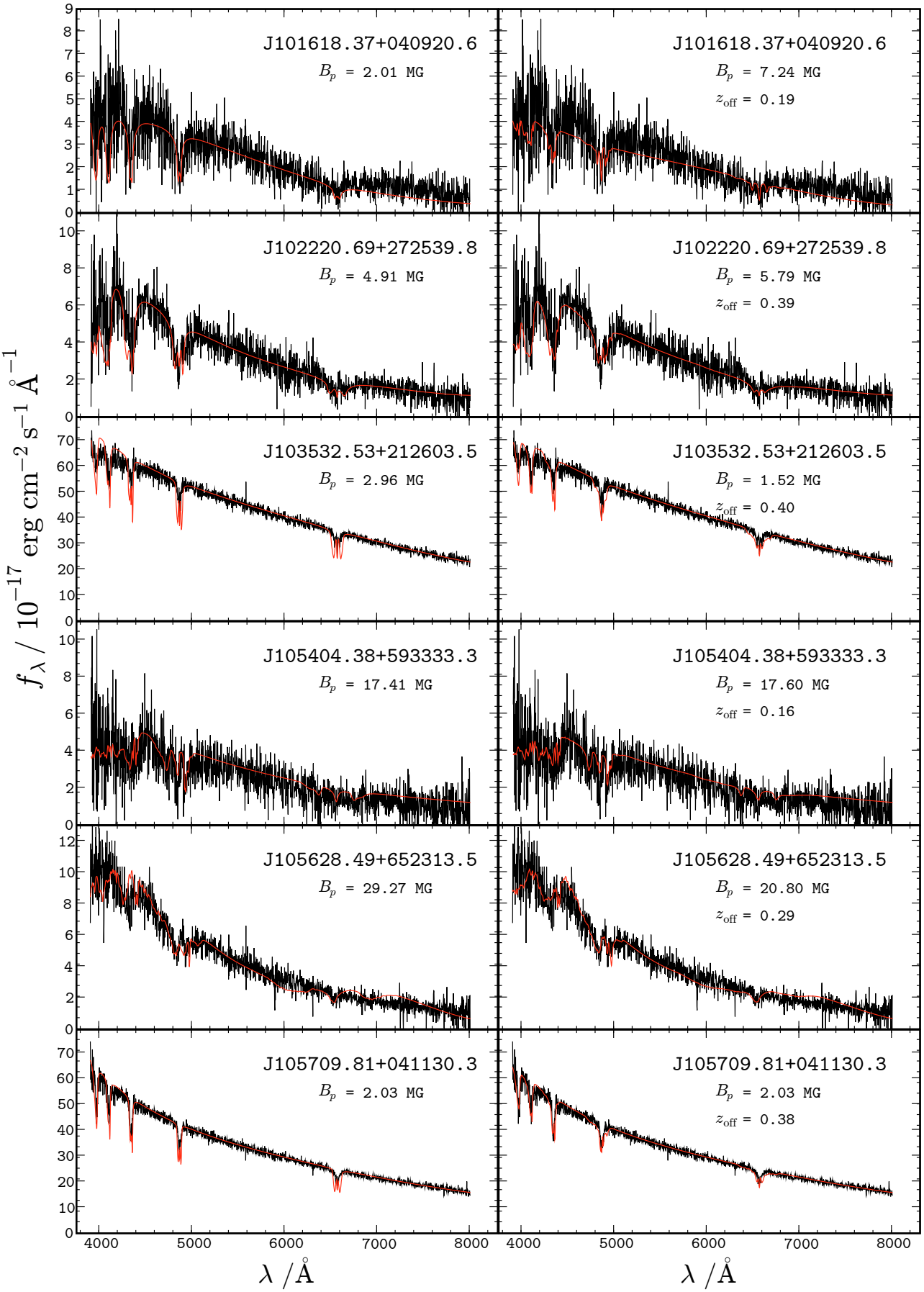


**Fig. A.11.** Fits of observed spectra of DAHs from the SDSS to centered magnetic dipoles with a polar field strength $B_{\rm p}$ (*left*) and dipoles shifted by $z_{\rm off}$ stellar radii along the dipole axis (*right*).

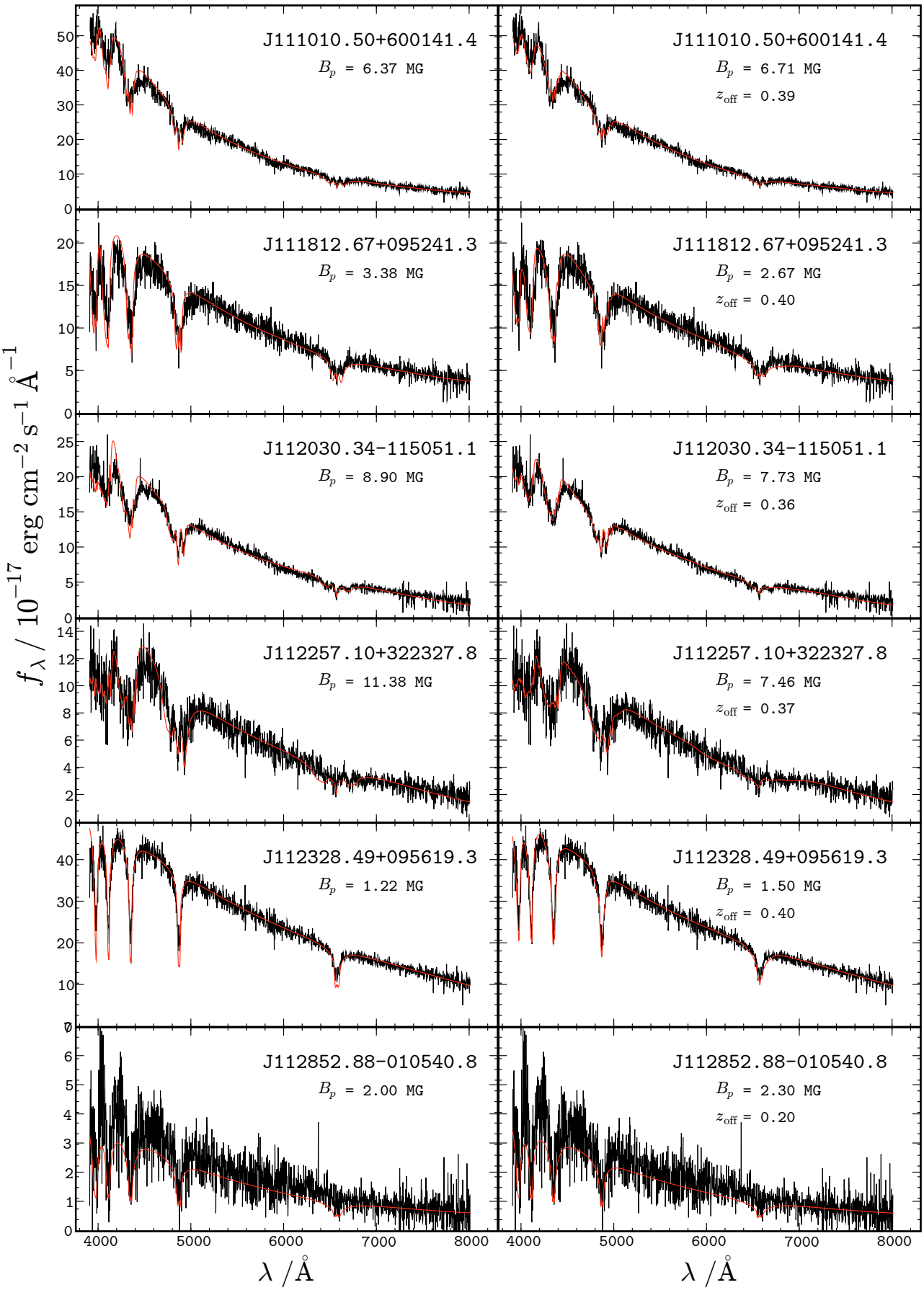


**Fig. A.12.** Fits of observed spectra of DAHs from the SDSS to centered magnetic dipoles with a polar field strength $B_{\rm p}$ (*left*) and dipoles shifted by $z_{\rm off}$ stellar radii along the dipole axis (*right*).

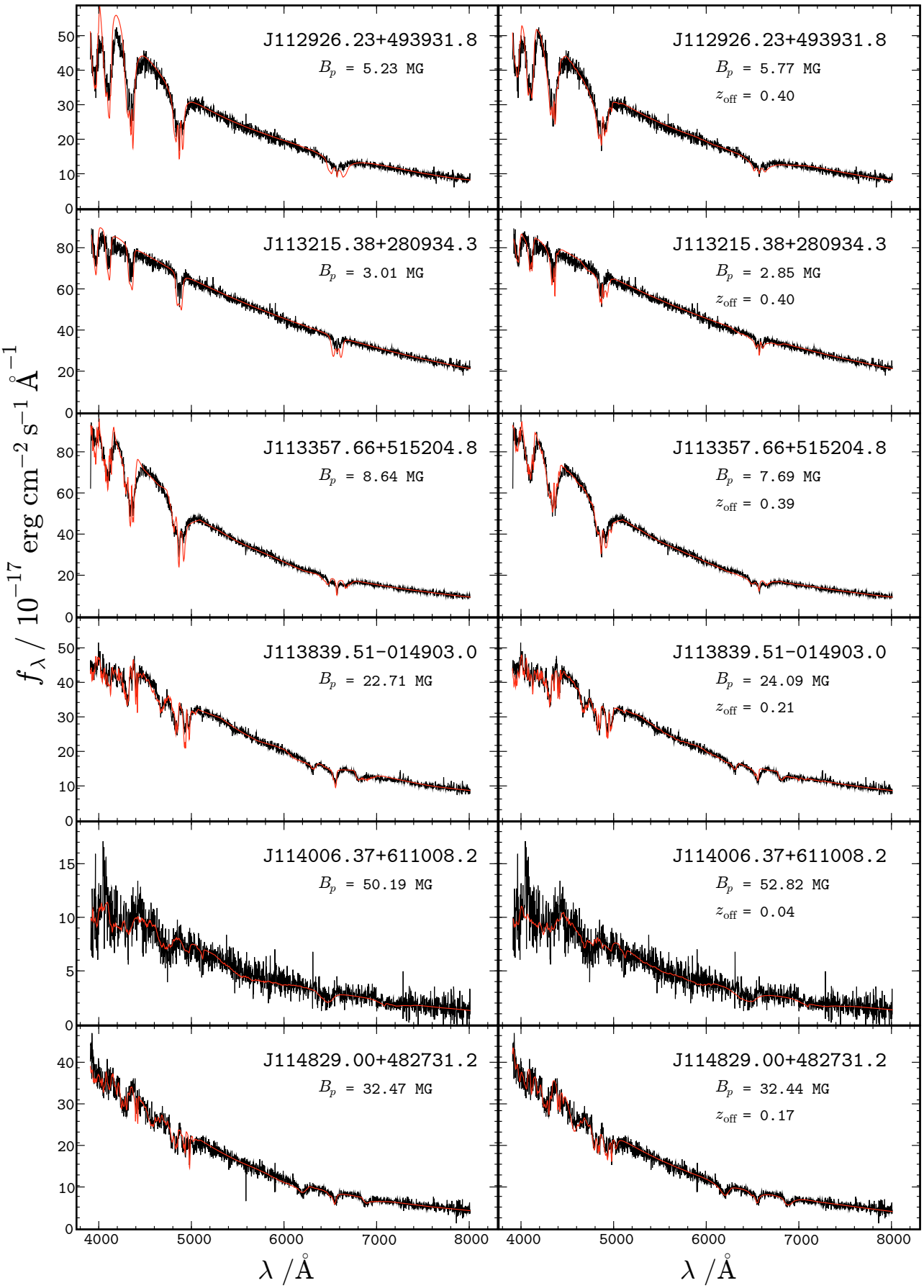


**Fig. A.13.** Fits of observed spectra of DAHs from the SDSS to centered magnetic dipoles with a polar field strength $B_{\rm p}$ (*left*) and dipoles shifted by $z_{\rm off}$ stellar radii along the dipole axis (*right*).

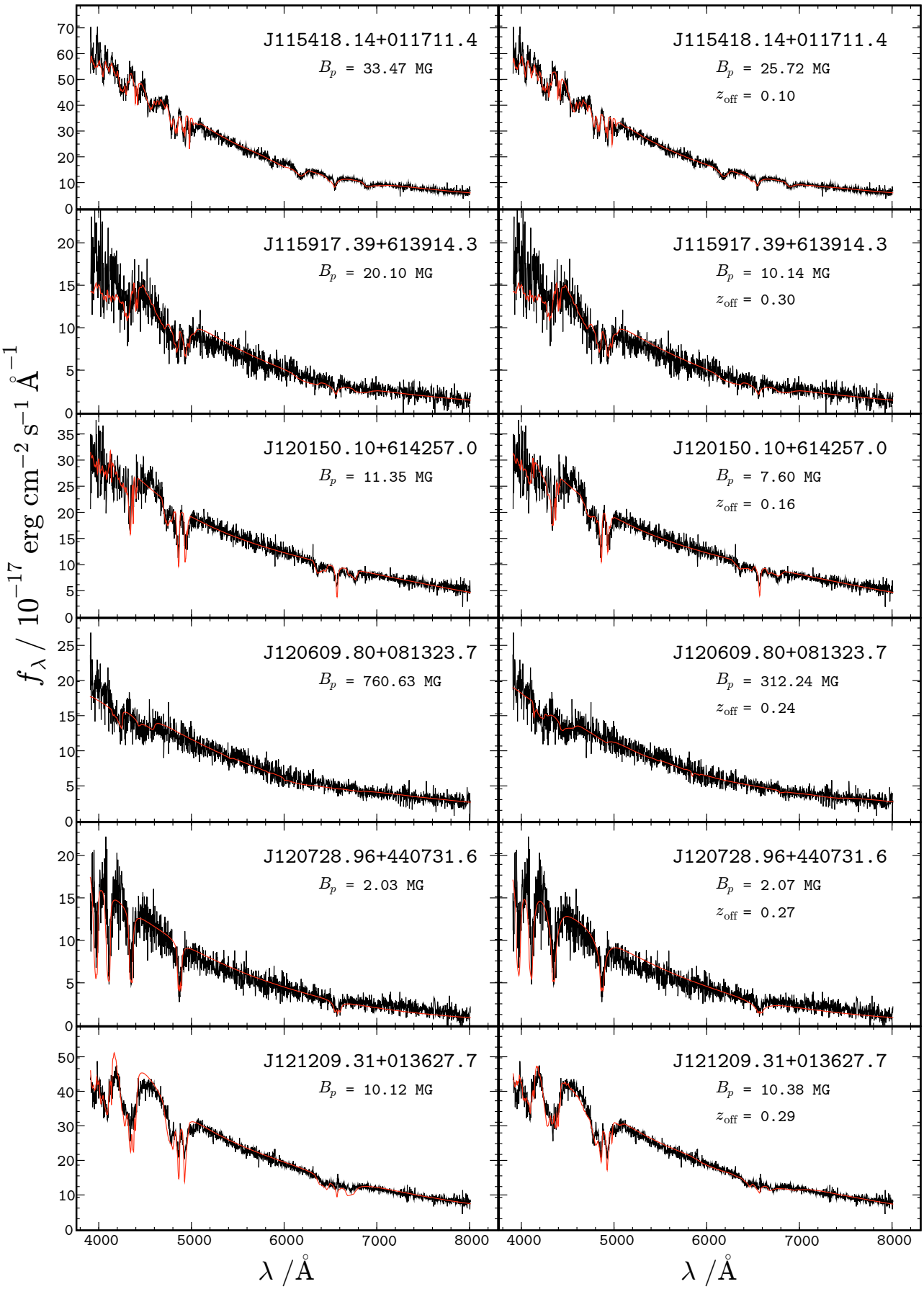


**Fig. A.14.** Fits of observed spectra of DAHs from the SDSS to centered magnetic dipoles with a polar field strength $B_{\rm p}$ (*left*) and dipoles shifted by $z_{\rm off}$ stellar radii along the dipole axis (*right*).

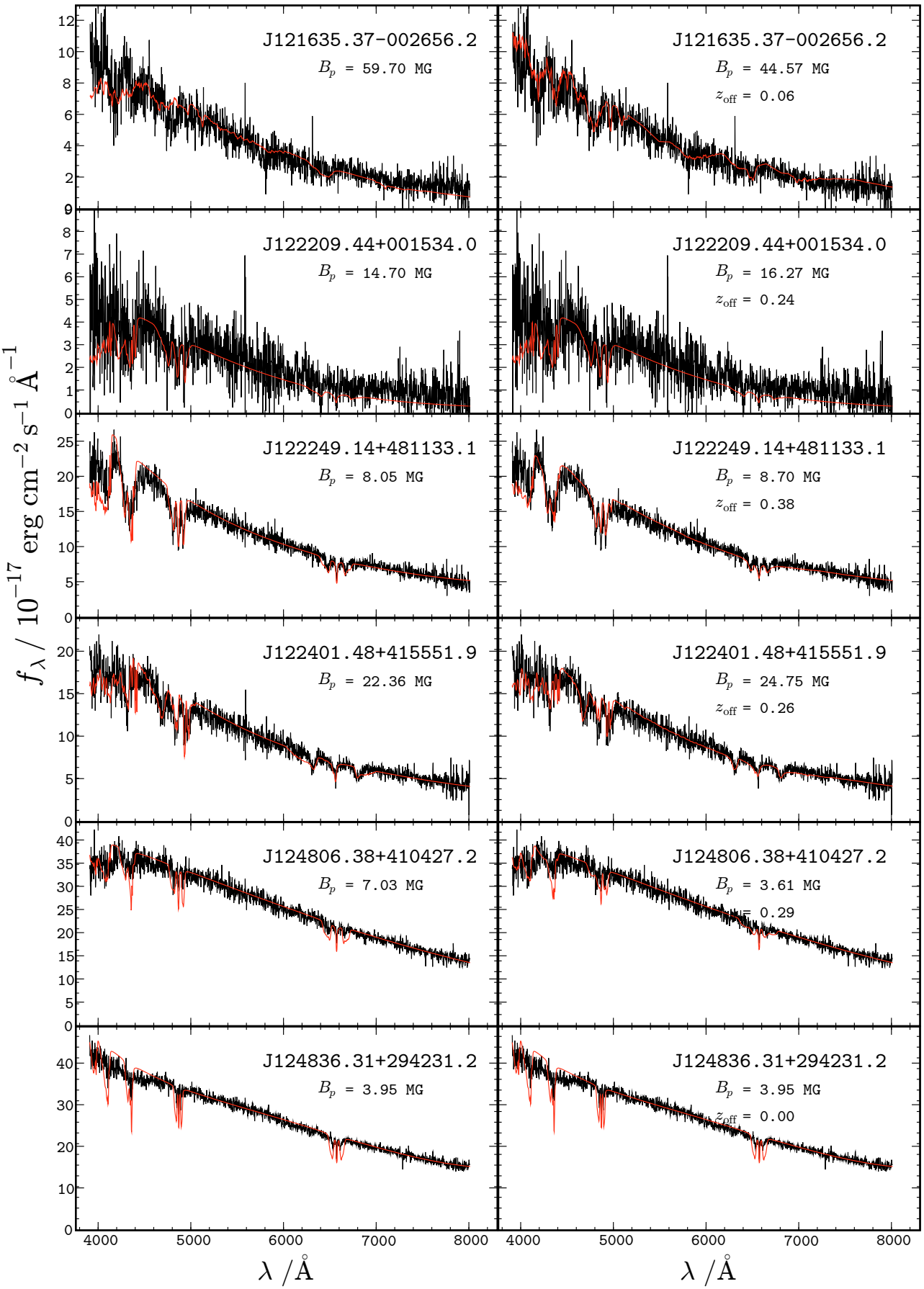


**Fig. A.15.** Fits of observed spectra of DAHs from the SDSS to centered magnetic dipoles with a polar field strength $B_{\rm p}$ (*left*) and dipoles shifted by $z_{\rm off}$ stellar radii along the dipole axis (*right*).

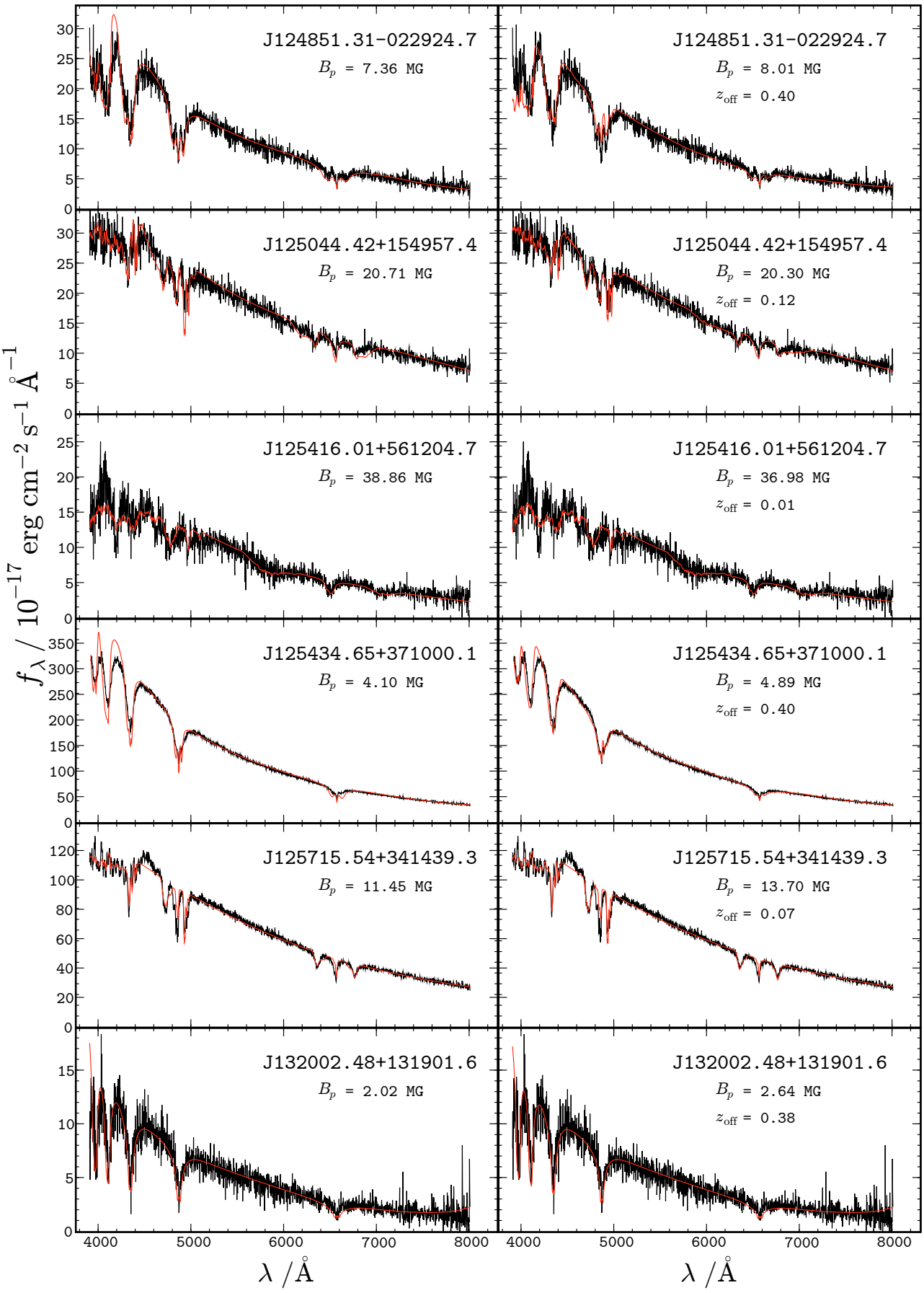


**Fig. A.16.** Fits of observed spectra of DAHs from the SDSS to centered magnetic dipoles with a polar field strength $B_{\rm p}$ (*left*) and dipoles shifted by $z_{\rm off}$ stellar radii along the dipole axis (*right*).

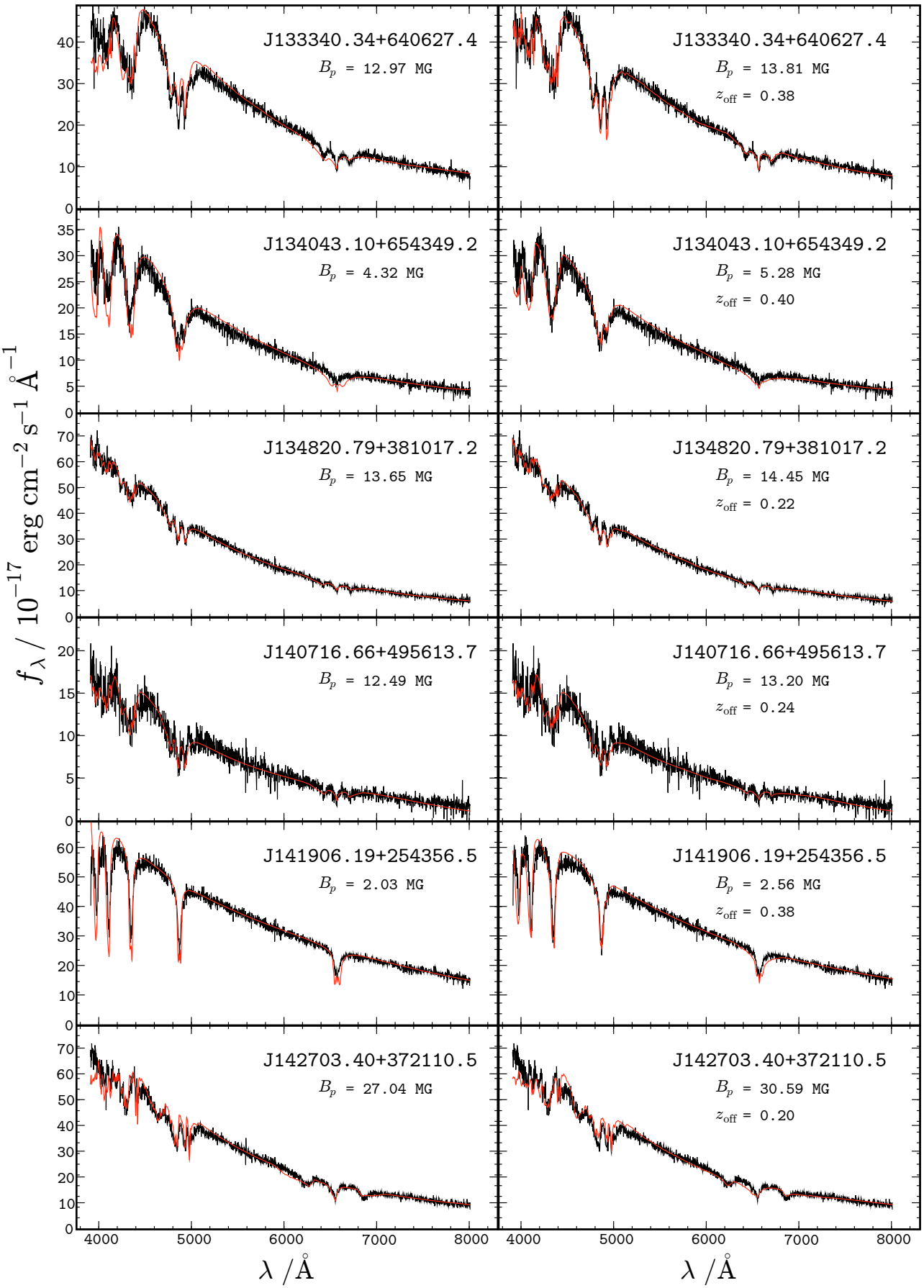


**Fig. A.17.** Fits of observed spectra of DAHs from the SDSS to centered magnetic dipoles with a polar field strength $B_{\rm p}$ (*left*) and dipoles shifted by $z_{\rm off}$ stellar radii along the dipole axis (*right*).

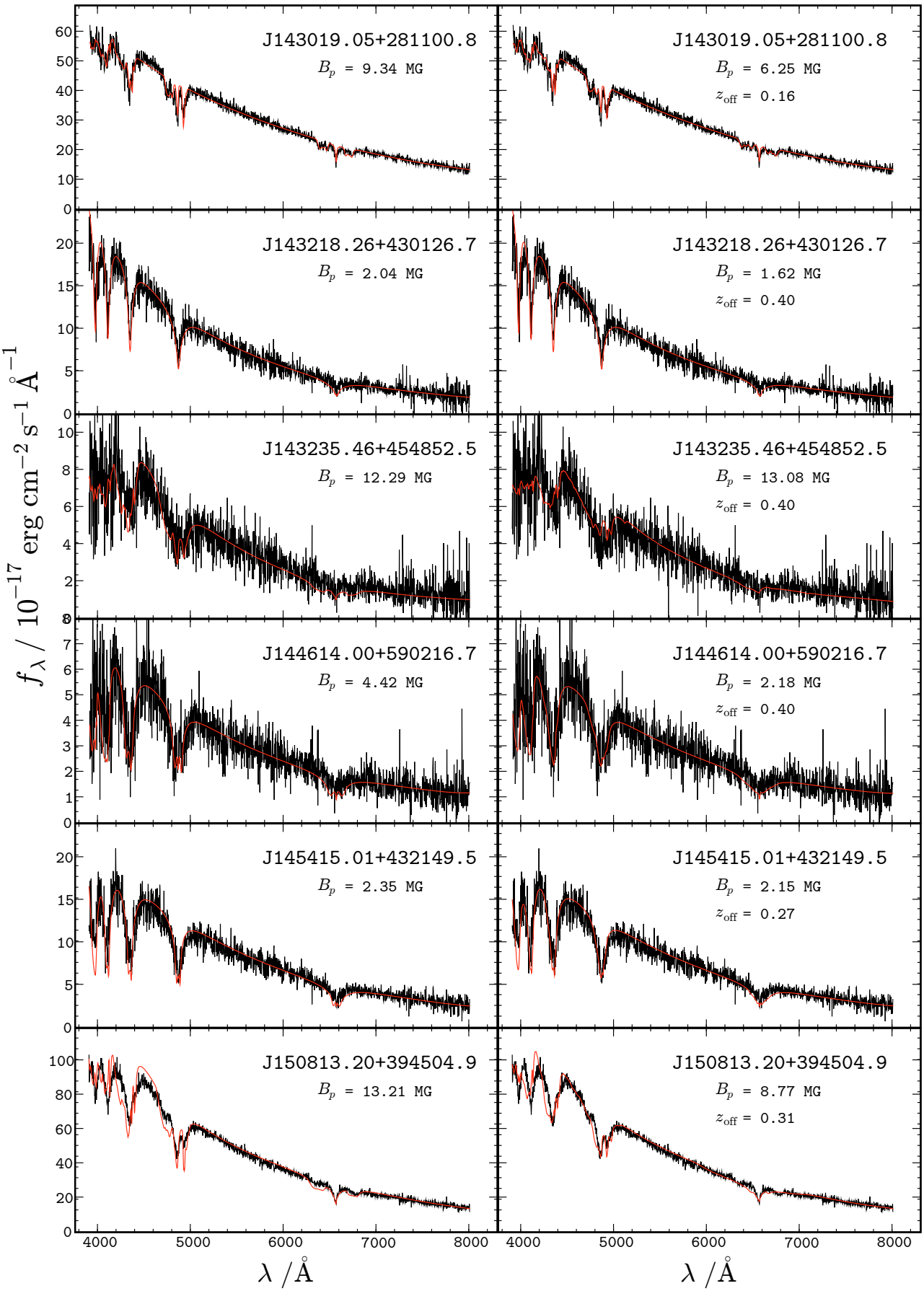


**Fig. A.18.** Fits of observed spectra of DAHs from the SDSS to centered magnetic dipoles with a polar field strength $B_{\rm p}$ (*left*) and dipoles shifted by $z_{\rm off}$ stellar radii along the dipole axis (*right*).

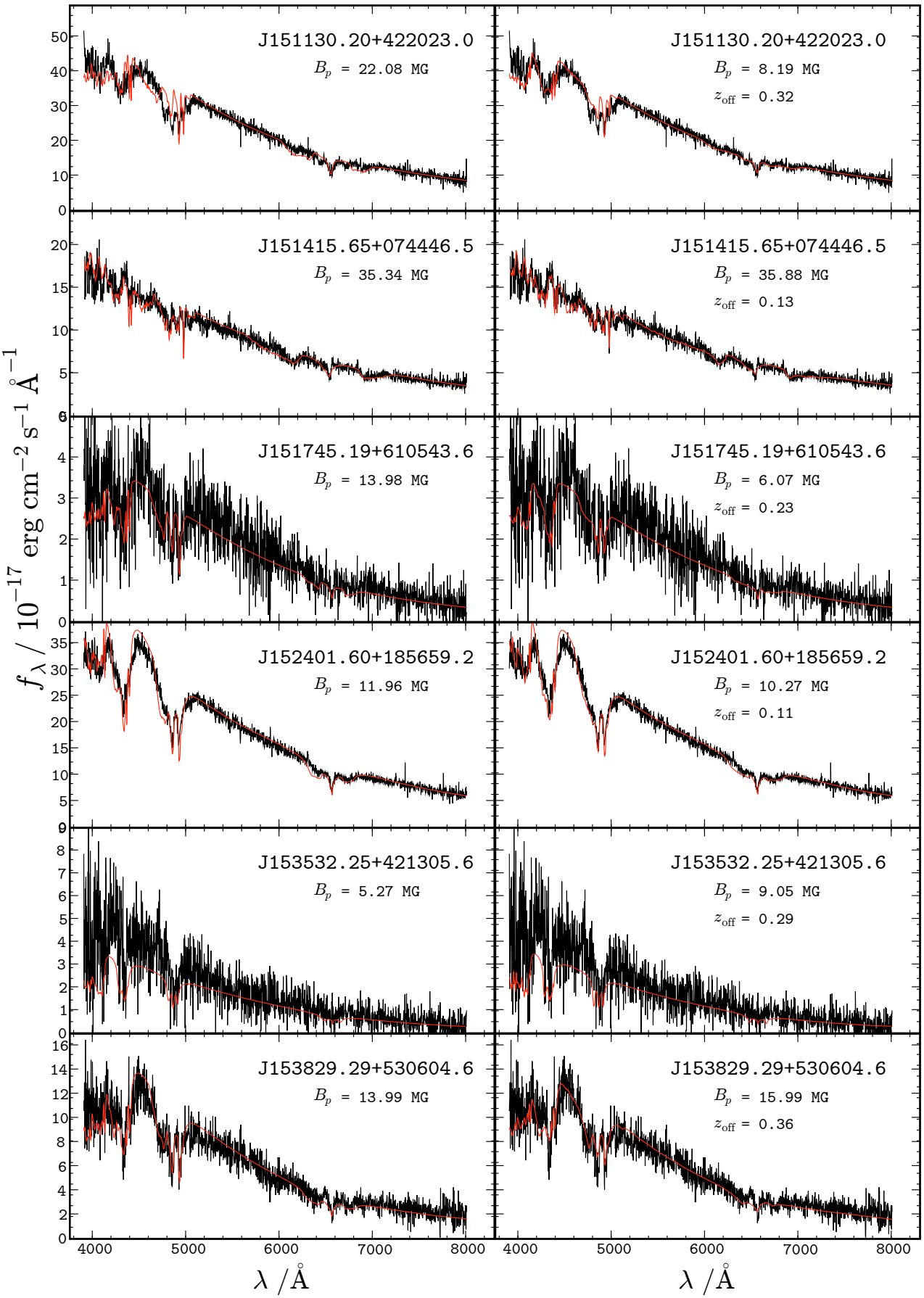


**Fig. A.19.** Fits of observed spectra of DAHs from the SDSS to centered magnetic dipoles with a polar field strength $B_{\rm p}$ (*left*) and dipoles shifted by $z_{\rm off}$ stellar radii along the dipole axis (*right*).

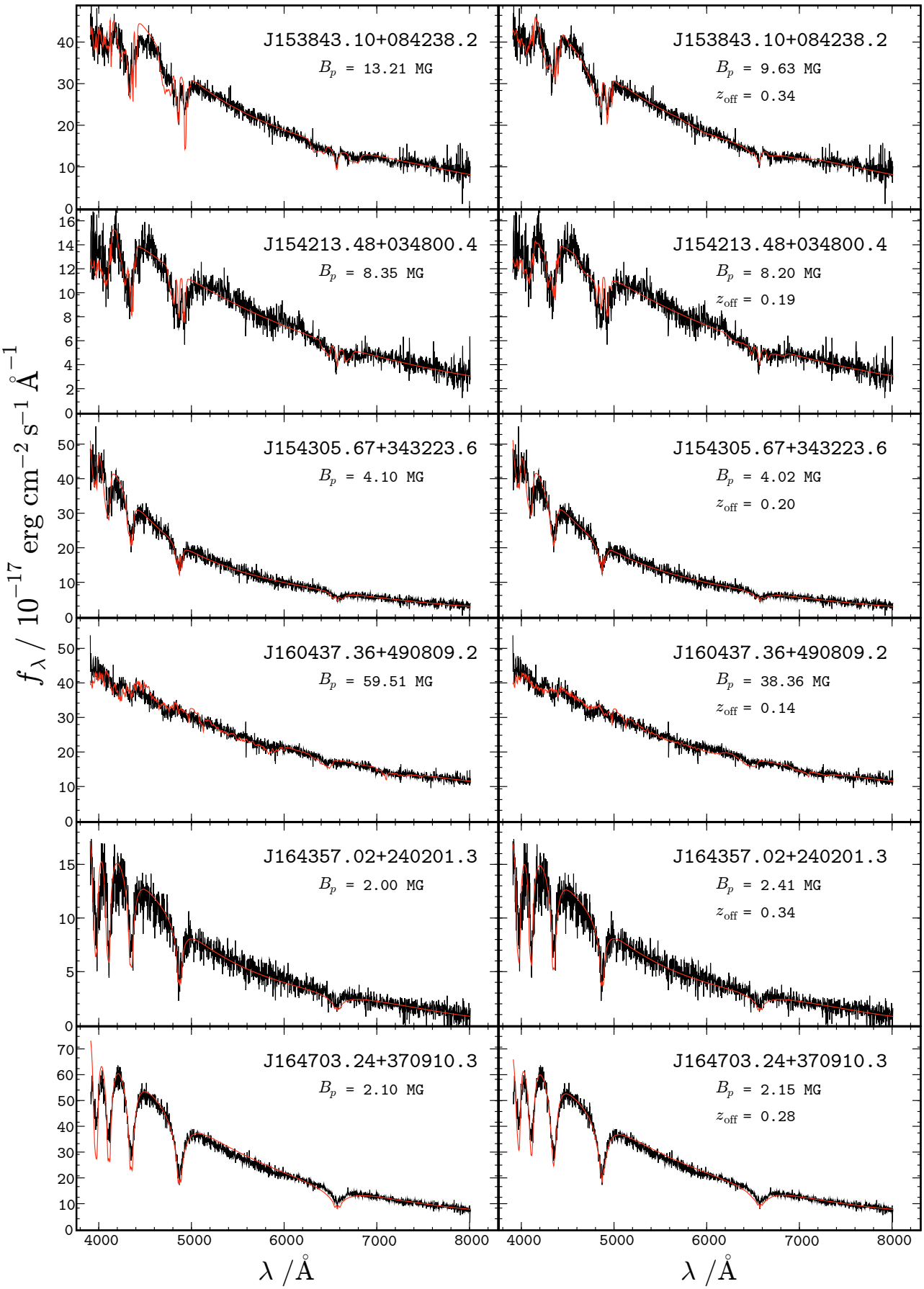


**Fig. A.20.** Fits of observed spectra of DAHs from the SDSS to centered magnetic dipoles with a polar field strength $B_{\rm p}$ (*left*) and dipoles shifted by $z_{\rm off}$ stellar radii along the dipole axis (*right*).

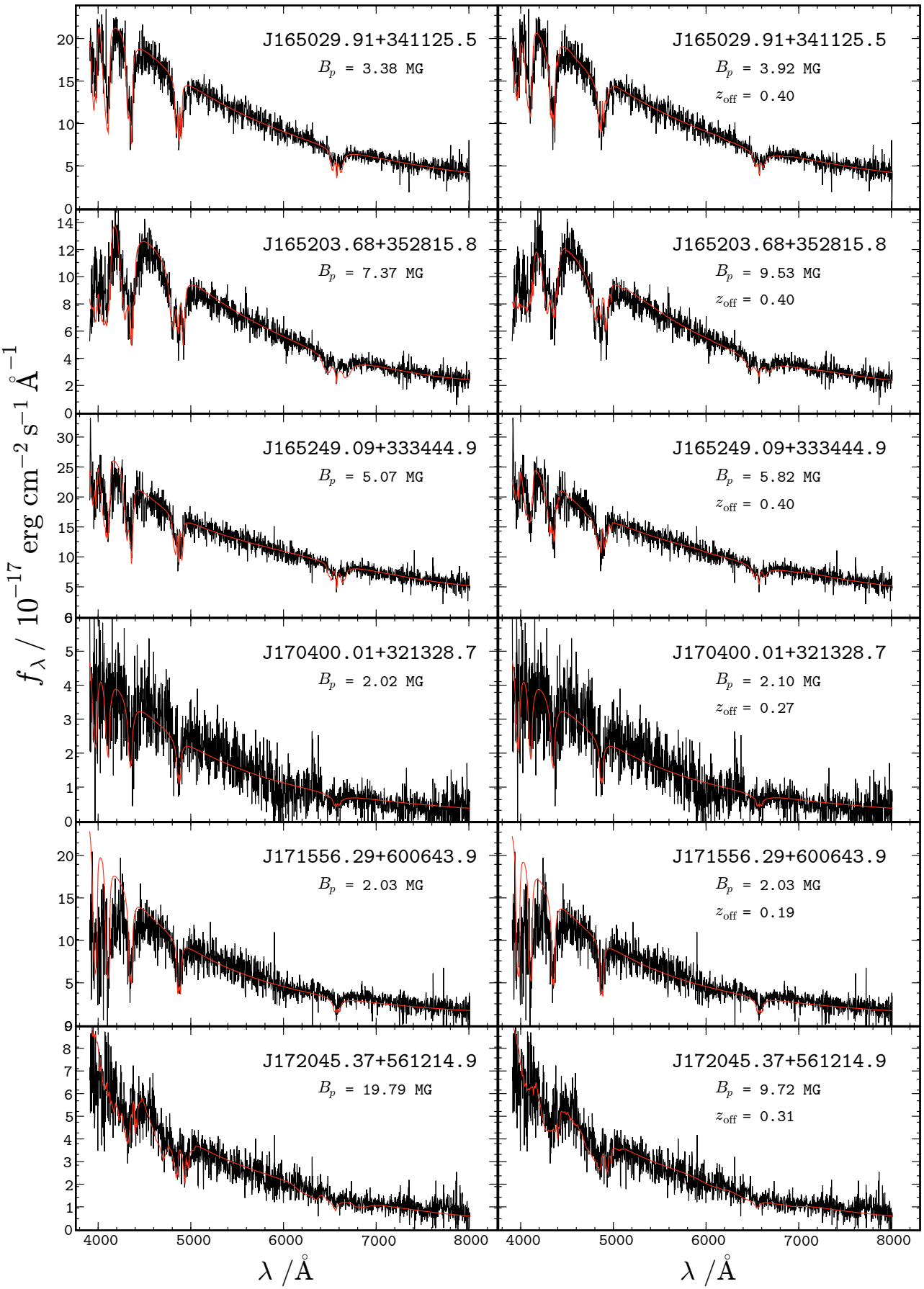


**Fig. A.21.** Fits of observed spectra of DAHs from the SDSS to centered magnetic dipoles with a polar field strength $B_{\rm p}$ (*left*) and dipoles shifted by $z_{\rm off}$ stellar radii along the dipole axis (*right*).

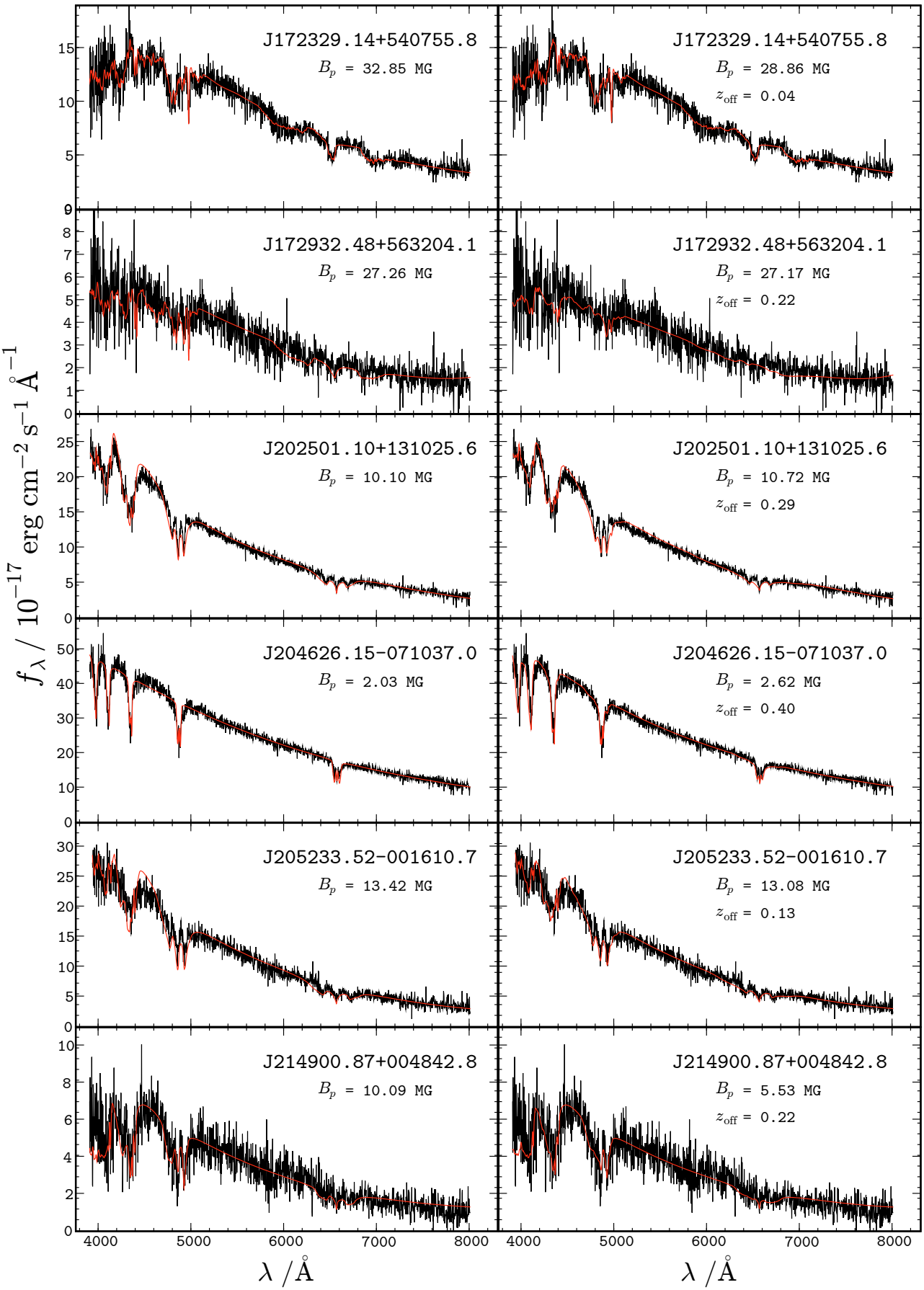


**Fig. A.22.** Fits of observed spectra of DAHs from the SDSS to centered magnetic dipoles with a polar field strength $B_{\rm p}$ (*left*) and dipoles shifted by $z_{\rm off}$ stellar radii along the dipole axis (*right*).

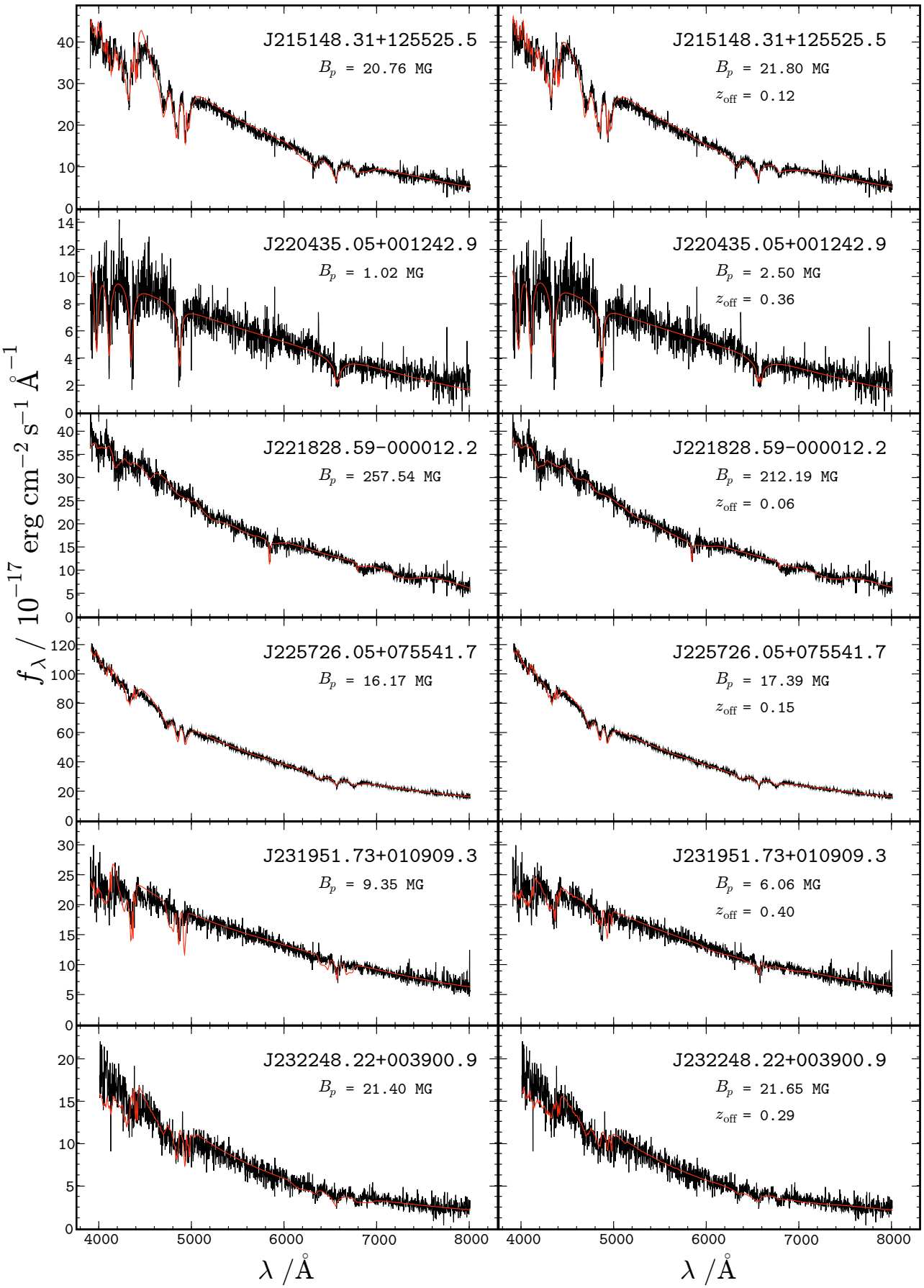


**Fig. A.23.** Fits of observed spectra of DAHs from the SDSS to centered magnetic dipoles with a polar field strength $B_{\rm p}$ (*left*) and dipoles shifted by $z_{\rm off}$ stellar radii along the dipole axis (*right*).

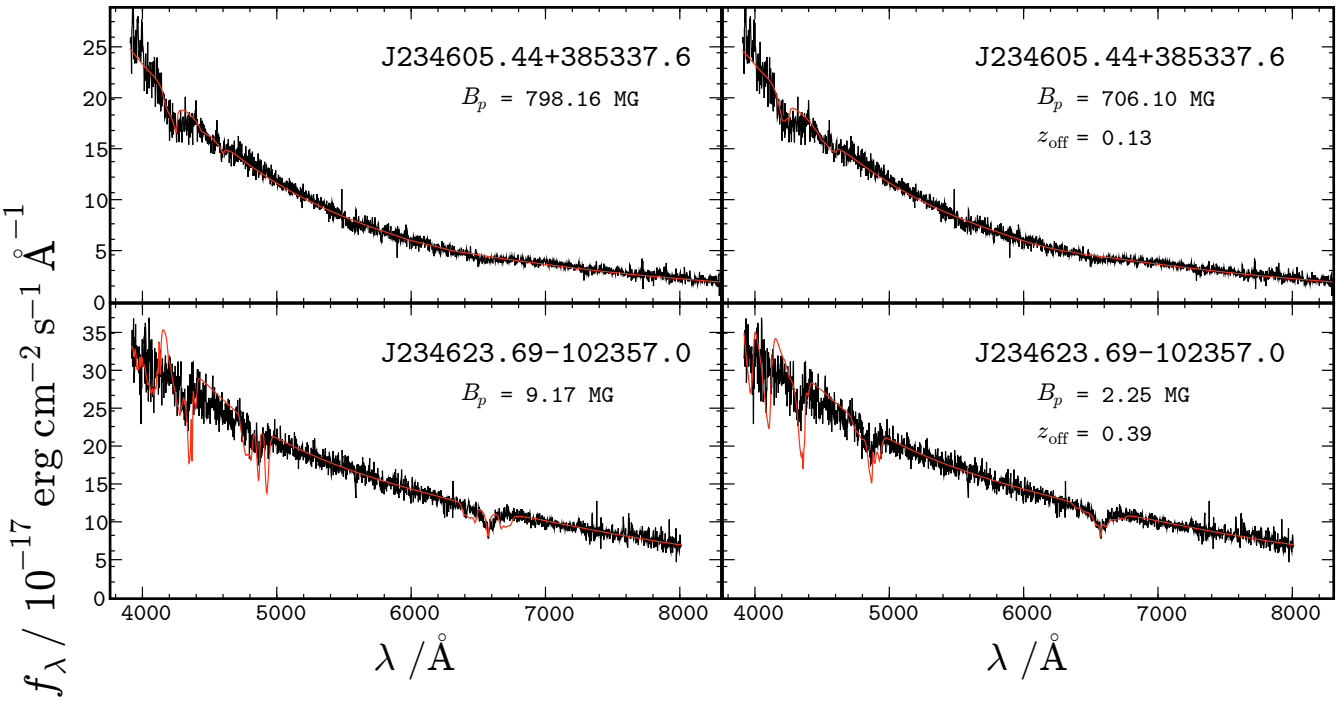


**Fig. A.24.** Fits of observed spectra of DAHs from the SDSS to centered magnetic dipoles with a polar field strength $B_{\rm p}$ (*left*) and dipoles shifted by $z_{\rm off}$ stellar radii along the dipole axis (*right*).